JGR Atmospheres

RESEARCH ARTICLE

10.1029/2024JD041307

# Large-Scale Statistically Meaningful Patterns (LSMPs) Associated With Precipitation Extremes Over Northern California

**Abhishekh Kumar Srivastava**[1], **Richard Grotjahn**[1], **Alan M. Rhoades**[2], and **Paul Aaron Ullrich**[1,3]

[1]Department of Land, Air and Water Resources, University of California, Davis, CA, USA, [2]Lawrence Berkeley National Laboratory, Berkeley, CA, USA, [3]Lawrence Livermore National Laboratory, Livermore, CA, USA

**Key Points:**

- A significance test finds the minimum number of robust weather pattern clusters for extreme precipitation over Northern California is four
- How significant and consistent parts of the weather patterns (essential parts of large-scale statistically meaningful patterns (LSMPs)) evolve are shown for multiple atmospheric variables
- Binary forecast skill tests of LSMPs identify variables to use in a new copula-based framework for probabilistic prediction of PEx events

**Supporting Information:**

Supporting Information may be found in the online version of this article.

**Correspondence to:**

A. K. Srivastava,
asrivas@ucdavis.edu

**Citation:**

Srivastava, A. K., Grotjahn, R., Rhoades, A. M., & Ullrich, P. A. (2025). Large-scale statistically meaningful patterns (LSMPs) associated with precipitation extremes over Northern California. *Journal of Geophysical Research: Atmospheres*, *130*, e2024JD041307. https://doi.org/10.1029/2024JD041307

Received 5 APR 2024
Accepted 9 JAN 2025

**Author Contributions:**

**Conceptualization:** Abhishekh Kumar Srivastava, Richard Grotjahn
**Formal analysis:** Abhishekh Kumar Srivastava
**Funding acquisition:** Paul Aaron Ullrich
**Investigation:** Abhishekh Kumar Srivastava
**Methodology:** Abhishekh Kumar Srivastava, Richard Grotjahn, Alan M. Rhoades
**Project administration:** Paul Aaron Ullrich
**Resources:** Richard Grotjahn, Paul Aaron Ullrich

**Abstract** We analyze large-scale statistically meaningful patterns (LSMPs) that precede extreme precipitation (PEx) events over Northern California (NorCal). We find LSMPs by applying k-means clustering to the two leading principal components of daily 500 hPa geopotential height anomalies two days before the onset, from October to March during 1948–2015. Statistical significance testing based on Monte Carlo simulations suggests a minimum of four statistically distinguished LSMP clusters. The four LSMP clusters are characterized as Northwest continental negative height anomaly, Eastward positive "Pacific-North American Pattern (PNA)," Westward negative "PNA," and Prominent Alaskan ridge. These four clusters, shown in multiple variables, evolve very differently and have differing links to the Arctic and tropical Pacific regions. Using binary forecast skill measures and a new copula-based framework for predicting PEx events, we find LSMP indices that are useful predictors of NorCal PEx events, with moisture-based variables being the best predictors of PEx events at least 6 days before the onset, and the lower atmospheric variables being better than their upper atmospheric counterparts any day in advance tested. To ensure statistical rigor, the LSMPs analyzed here (with the modified acronym) include local tests of both significance and consistency, which are not always featured in the literature on large-scale meteorological patterns.

**Plain Language Summary** Like some other weather extremes, extreme precipitation events can be organized and triggered by large-scale circulation patterns (horizontal span > 1,000 km) in several variables. Each of these events clusters around one of a minimum of four distinct collections of large-scale circulation patterns that evolve to cause extreme precipitation over Northern California. Although these four clusters have a common low-pressure system near Northern California at event onset, they differ from each other in the orientation, evolution, and spatial extent of low- and high-pressure systems over a much larger region. Each cluster has different links to properties in distant regions, such as the tropical Pacific Ocean and Alaska, as well as regions in between. We construct indices from statistically significant and commonly occurring parts of these collections. Such indices are useful large-scale predictors of smaller-scale extreme precipitation events with atmospheric moisture-based variables being the best predictors.

## 1. Introduction

Extreme precipitation (PEx) over California is marked by a large interannual variability (Dettinger et al., 2011). For example, record rainfall during the winter of 2016–2017 was followed by record dry conditions in the fall and winter of 2017–2018 (Gershunov et al., 2017). Such a large variability in rainfall is a concern from both drought (Shukla et al., 2015; Swain et al., 2014) and flood perspectives (e.g., Feb 2017 Oroville Dam disaster; White et al., 2019). Projections of future precipitation suggest an increase in high-intensity precipitation extremes and a further enhancement in interannual variability (Polade et al., 2017; Rhoades et al., 2020; Swain et al., 2018). Since changes in PEx over California have severe impacts on activities such as water management, dam protection, and agriculture, it is important to understand both the large and small-scale patterns associated with PEx over California. Although small-scale local features (e.g., local orography and moisture ascent) pose problems for climate models due to limitations such as inadequate horizontal and vertical resolutions, imperfect parameterizations, and cloud microphysics, large-scale circulation mechanisms are largely reproduced in climate model simulations (e.g., Agel & Barlow, 2020; Boroneant et al., 2006; DeAngelis et al., 2013; Gutowski et al., 2003). This study explores the large-scale circulation patterns associated with PEx events over Northern California (NorCal).

**Software:** Abhishekh Kumar Srivastava, Alan M. Rhoades, Paul Aaron Ullrich
**Supervision:** Richard Grotjahn, Paul Aaron Ullrich
**Validation:** Abhishekh Kumar Srivastava, Richard Grotjahn, Paul Aaron Ullrich
**Writing – original draft:** Abhishekh Kumar Srivastava, Richard Grotjahn
**Writing – review & editing:** Abhishekh Kumar Srivastava, Richard Grotjahn, Alan M. Rhoades, Paul Aaron Ullrich

Large-scale meteorological patterns, also called large-scale statistically meaningful patterns (LSMPs), associated with extreme events are the synoptic-scale atmospheric and surface conditions that precede the events (e.g., PEx, extreme heat, or cold-air outbreaks). LSMPs are different from teleconnections (e.g., the El Niño-Southern Oscillation (ENSO)) in several ways. First, LSMPs can be high-frequency patterns based on instantaneous data (as in this report). Second, LSMPs are the specific meteorological patterns that occur in connection with an extreme event type, whereas teleconnections are recurring, slowly evolving, persistent, large-scale patterns (also known as low-frequency modes of variability) that can be defined without any reference to extremes (Barlow et al., 2019). Although local factors such as lifting, static stability, and moisture availability control the intensity and duration of PEx (e.g., Moore et al., 2020; Neiman et al., 2002), LSMPs that determine or control these factors vary with season, region, and definition of an extreme event.

As outlined in Grotjahn et al. (2016), multiple methods can identify large-scale circulation features associated with an extreme event. A common method is the construction of composited maps of meteorological variables conditioned on the occurrence of an extreme event type (Collow et al., 2016, 2020; DeAngelis et al., 2013; Gao et al., 2014; Grotjahn & Faure, 2008). Compositing-based studies show that the precipitation days over NorCal are locally associated with a low-pressure system and associated extratropical cyclones in the Northern Pacific off the west coast of the United States (e.g., Gao et al., 2014; Grotjahn & Faure, 2008; Neiman et al., 2008). These weather systems act to channel winds and moisture into narrow structures called atmospheric rivers (ARs) (Newell et al., 1992; Ralph et al., 2006; Zhu & Newell, 1998) that are directed toward the coast to produce precipitation over land (Fish et al., 2022; Lamjiri et al., 2017; Smith et al., 2010). Another strong feature of these large-scale patterns is the zonally elongated jet over the North Pacific further extended toward the west coast of the United States (Payne & Magnusdottir, 2014).

However, when looking at large scales, locally persistent low-pressure systems are found to be embedded in different circulation patterns, suggesting that there could be more than one large-scale pattern that can be associated with PEx events over NorCal. Popular methods that can identify these different circulation features are: empirical orthogonal function (EOF) analysis (Guirguis et al., 2018, 2020), self-organizing maps (SOMs; Guirguis et al., 2019; Loikith et al., 2017), and clustering analysis (Agel et al., 2018; Fish et al., 2022; Moore et al., 2021; Zhao et al., 2019). Loikith et al. (2017) demonstrated that the majority of the DJF PEx days over Northern California occur for SOM node 1 (followed by node 5), identified by a surface low pressure centered to the northwest of the northwestern continental United States, a 500 mb geopotential height (Z500) trough axis offshore, and the main axis of the 250 mb jet zonally oriented over central California. Guirguis et al. (2020), using SOM analysis, demonstrated that wet and dry conditions over California result from interactions between four North Pacific circulation regimes (their NP4 regimes) on daily timescales. D. Chen et al. (2021) found that their "California precipitation mode," identified as the third principal component (PC) of the Z500 field, is closely linked to California extreme precipitation days. Guirguis et al. (2019) used nine SOM nodes trained on Z500 anomalies to characterize different types of landfalling ARs at 40°N impacting NorCal. They showed that these different AR types occur during different phases of large-scale teleconnection patterns such as ENSO, Pacific decadal oscillation (PDO), and Pacific North American (PNA) pattern. It is worth noting that some of the nine chosen SOM nodes shared spatiotemporal commonalities and might not have been statistically distinct from one another. Fish et al. (2022) identified six clusters of large scale patterns associated with AR events affecting California and explored the frequency of clusters during the ENSO phases. Moore et al. (2021) found four categories of large-scale atmospheric patterns for long-duration (>7 days) heavy precipitation events over the West Coast of the United States. Out of these four categories, two are identified by a strong zonal jet stream over the eastern North Pacific, and the two other patterns are identified by atmospheric blocking over the central North Pacific and the Bering Sea-Alaska region, respectively.

These studies provide useful information about how PEx forms over NorCal. Nonetheless, there are five aspects of research methodology to consider. First, there is a misconception about what constitutes an LSMP. As elaborated in Grotjahn (2011), an LSMP of a relevant variable, often meteorological (e.g., 500 mb geopotential height anomaly field) is more than some aggregate field; it also must indicate what is important in the field. Therefore, an LSMP includes two additional integral features: significance and consistency. The significance establishes if an anomalous pattern (e.g., sea surface temperature anomaly) statistically differs from what occurs by chance. Consistency, as the name suggests, refers to how often an anomaly of the same sign occurs at a grid point or location. Previous studies showing aggregate patterns often overlook the consistency assessment. We argue that significance and consistency are integral parts of an LSMP for two reasons: (a) High significance does not guarantee high consistency (e.g. Grotjahn & Faure, 2008 and (b) any future changes in either significance or consistency may suggest dynamical changes impacting the occurrences of extremes. Second, a majority of previous studies have considered a small spatial domain around NorCal. However, as the name suggests, LSMPs are large-scale patterns (and may show far teleconnections, too) that may not be fully captured by such small domains. Third, what is the minimum number of LSMP clusters necessary to best describe northern California's PEx events? This question has direct relevance for climate model evaluation, as any model expected to reasonably simulate PEx should be able to reproduce the spatial pattern and frequency of each observed clustered pattern. Fourth, most studies use concurrent meteorological conditions (same day) for identifying and clustering large-scale patterns associated with PEx events (e.g., Barlow et al., 2019). Analogous to NorCal heat waves, which have a similar pattern at their onset that is arrived upon from two different synoptic evolutions (Lee & Grotjahn, 2016), NorCal PEx events might also be arrived at by more than one synoptic evolution. Indeed, Figure 6 in Grotjahn and Faure (2008) implies more than one pattern as individual events have a highly significant Alaskan ridge, whereas other events have a deep trough over Alaska. From causal and predictability perspectives, the relevant LSMPs should be identified from the meteorological conditions persisting before the event. Fifth, although a limited number of studies have shown the predictability of PEx events using LSMPs as predictors (e.g., Gao & Mathur, 2021), a comprehensive approach for probabilistic predictions of precipitation using LSMPs as predictors is missing.

In this work, we examine the LSMPs associated with PEx over NorCal to address the limitations mentioned above. A PEx event is defined here as the 24-hr precipitation total of more than the $95^{th}$ percentile of the daily precipitation averaged over a region of NorCal. We also present a copula-based framework for making probabilistic predictions of precipitation. Broadly, our main objectives are:

1. Identify clusters of LSMPs that persist before the onset of the PEx over NorCal;
2. Statistically estimate the minimum number of distinguishable LSMP clusters leading to PEx events over NorCal;
3. Examine the evolution of a comprehensive list of meteorological LSMPs leading to the PEx event onset;
4. Use a copula-based framework to make a probabilistic prediction of PEx events over NorCal using LSMP indices as predictors.

The LSMP clusters are identified by applying the k-means clustering algorithm to the two leading principal components of the 500 hPa daily geopotential height anomalies (Z500) two days before the onset (lag 2). Along with the Z500, we show the evolution of LSMPs associated with the other related quantities such as 850 hPa and 300 hPa velocity fields, streamfunctions at 300 and 850 mb, surface temperature, integrated vapor transport (IVT), and surface pressure.

This paper strongly complements the paper by Moore et al. (2021), which focused on synoptic dynamics during 7-day-long PEx events impacting NorCal. Here, we focus on predictability, remote connections, and the creation of 1-day or longer PEx events impacting the same region. Although Moore et al. (2021) include all events, we include only the largest precipitation day in a multi-day precipitation event and exclude “mixed” events which cannot be clearly assigned to a single cluster. We do this to have more distinct clusters and are enabled to do so because we have larger sample sizes. Our patterns are sharper because we are combining ’instantaneous' fields. In contrast, the fields for each event in Moore et al. (2021) are smoothed by their time averaging, during which weather systems move across their domain. We also employ a rigorous test to see the minimum number of clusters needed for them to be significantly different. We search for LSMPs over a larger region and, in so doing, find distant connections not found within original focus region of Moore et al. (2021). Although Moore et al. (2021) present the significant parts of patterns, we apply a more complete LSMP analysis, including applying significance and consistency tests at each grid point, which are critical for assessing predictability. Following this introduction, the data and methods are discussed in Section 2, results in Section 3, and an overall summary is in Section 4.

## 2. Data and Methods

In this study, we use daily 0.25° × 0.25° precipitation data over 1948–2015 from the National Oceanic and Atmospheric Administration Climate Prediction Center (CPC) Unified CONUS data set (CPC; M. Chen et al., 2008; Xie et al., 2007) to identify PEx events over the NorCal region. The gridded CPC data are constructed from the quality-controlled station data using the optimal interpolation (OI) algorithm, which exhibits relatively small degradation in performance statistics over regions covered by fewer gauges. Previous studies suggest that the performance of the CPC data set in capturing different aspects of extreme precipitation is similar to the other high-resolution gridded data sets (e.g., Akinsanola et al., 2020; Srivastava et al., 2020; Timmermans et al., 2019). To identify extreme precipitation events, we first calculate the 24-hr spatially averaged precipitation $\bar{P}$ by taking the mean of 24-hr nonzero precipitation values (i.e., $P > 0$ mm/day) at each grid point across the NorCal region defined as 124.5°W to 119.25°W and 38.69°N to 43.17°N. A PEx event is identified if a 24-hr $\bar{P}$ magnitude exceeds the $95^{th}$ percentile of $\bar{P}$ values over 1948–2015. This criterion identifies a total of 489 daily precipitation events. However, some of these events are on consecutive days. Since such events on consecutive days are not exclusively independent, we pick the largest precipitation day in a 3-day period. This procedure reduces the total number of exclusive events to 311. The PEx dates, along with cluster assignments, are listed in Supporting Information S1.

For the LSMP analysis, we use the NOAA-CIRES-DOE Twentieth Century Reanalysis version 3 (20CRv3, 1836–2015; Slivinski et al., 2019). The 20CRv3 uses an Earth system model to assimilate surface pressure observations with prescribed lower boundary conditions from observed sea surface temperature and sea-ice concentrations and bounded by prescribed radiative forcing to generate a four-dimensional global reanalysis product. Compared to its predecessor, 20CRv2c, the 20CRv3 uses upgraded assimilation methods, including an adaptive inflation algorithm, a higher resolution forecast model and a larger set of pressure observations. These improvements remove spin-up effects in the precipitation fields, reduce sea-level pressure bias, and improve the representation of storm intensity in the reanalysis product (Slivinski et al., 2019).

We use 20CRv3 because it provides a long period of data by consistently assimilating long-term surface observations while avoiding inconsistencies found in reanalysis products (e.g., long-term trends) arising from changing observational data sets (Fujiwara et al., 2017; Long et al., 2017; Slivinski et al., 2019). The feasibility of "reanalysis using only surface pressure data" is investigated by Compo et al. (2006) who report that "by using an advanced data assimilation system based on an ensemble Kalman filter, it would be feasible to produce high-quality maps of even the upper troposphere using only surface pressure observations." Slivinski et al. (2021), in their analysis of 20CRv3 find that upper-air fields from 20CRv3 in the late twentieth century and early twenty-first century correlate well with full-input reanalyses, and the correlation is predicted by the confidence fields from 20CRv3. They also state that the skill of analyzed 500 hPa geopotential heights from 20CRv3 for the period 1979–2015 is comparable to that of modern operational 3–4-day forecasts, and 20CRv3 performs well on climate timescales. Slivinski et al. (2021) also note that biases in some variables become substantial above 300 hPa, so we restrict our analysis to lower levels. To further investigate if 20CRv3 produces middle atmospheric fields comparable to the full reanalyses, we compare the temporal evolution of IVT over 1970–2015 in 20CRv3 with that in ERA5. We choose IVT for the comparison as IVT is a moisture-based field that includes contributions from specific humidity, surface pressure, zonal and meridional winds, and hence, it is a good indicator of the performance of 20CRv3 in capturing middle-to-lower atmospheric circulation patterns. Indeed, we show below that IVT emerges as the single best predictor of PEx events. We find that the total IVT fields (as well as IVT anomalies and LSMPs) during the PEx events are strikingly similar in the two data sets, with the spatial correlation between the two data sets being 0.98 or higher for all four clusters. Relevant Figures S1–S12 are included in Supporting Information S2.

In this study, we analyze the following variables from 20CRv3: surface pressure ($P_s$), surface temperature ($T_s$), IVT ($IVT$), horizontal and vertical velocity fields ($U, V, \omega$), atmospheric temperature ($T$), geopotential height ($Z$) and streamfunction ($\psi$) at 300, 500, and 850 hPa levels. We compute the daily anomalies of these variables by simultaneously regressing out the annual cycle and linear trend from the daily data over the period 1948–2015. Though not shown here, this approach of removing the annual cycle and trend from the data ensures that no residual trend or annual cycle remains present in the final anomaly product.

### 2.1. Clustering Procedure

For the clustering analysis, we apply a k-means clustering algorithm to the two leading PCs of the 500 hPa geopotential height anomalies two days before (lag 2) $\left(Za_{l2}^{500}\right)$ the event onset. The cluster domain is 180°W to 100°W and 25°N to 75°N. The two leading PCs explain around 54% of the variance. We estimate the significance of clusters using a Monte Carlo procedure following Straus (2018), described as follows. For each chosen number of clusters ($k = 1, 2, 3\ldots$ etc.), we compute the variance ratio ($R = \Delta/S$) for the first two PCs of $Za_{l2}^{500}$, where, $\Delta$ is the spread among the cluster centroids (also called between-sum-of-squares) and $S$ is the spread within clusters (also called total-within-sum-of-squares). In cluster analysis, we seek to minimize the spread within clusters, $S$. A maximum of the variance ratio $R$ corresponds to a minimum of $S$. We repeat the above-mentioned procedure 100 times with synthetic data sets. The synthetic data sets are generated from the multivariate Gaussian distribution computed using the same mean and covariance as in the data (here, the two leading PCs). For each iteration, we compute $R_{sample} = \Delta/S$. Finally, the $99^{th}$ percentile of the 100 $R_{sample}$ values, $(R_{sig})$ is computed. If $R > R_{sig}$ for a particular $k$, the clusters are declared significant and different from those occurring by chance. This procedure is repeated for $k = 1:7$. A similar procedure is also applied in Amini and Straus (2019). This process leads us to identify 4 significant clusters of $Za_{l2}^{500}$. For simplicity, we call the clusters $LZ_{l2}$ to indicate that the clusters are formed from $Za^{500}$ fields at lag 2. For each cluster, the cluster centroid $\left(\overline{LZ}_{l2}^{c}\right)$ is computed by taking the mean of all cluster members $1\ldots n_c$:

$$\overline{LZ}_{l2}^{c} = \frac{\sum_{n=1}^{n_c} Za_{l2,n}^{500}}{n_c}, \tag{1}$$

where, $\sum$ denotes summation over all cluster members, $n = 1\ldots n_c$, in a cluster $c$.

We clarify that we choose the first two PCs of $Za_{l2}^{500}$ for clustering as we do not try to explain a large fraction of variance (say, 80%); rather, we focus on the largest scale features of $Za^{500}$ and assess clusters with respect to those phenomena. Another objective reason to choose only two PCs with 54% variance explained is concerned with the variance ratio $R$ defined above. The variance ratio $R$ can also be regarded as a signal-to-noise ratio (Straus et al., 2017). Figure S13 in Supporting Information S2 shows $R$ computed from PC truncations 1 to 4. As the figure suggests, the signal-to-noise ratio ($R$) computed from the first two PCs is significant for clusters 3 and more. However, using three or more PCs does not guarantee the significance of $R$ for clusters 3 and beyond, possibly because of the addition of more noise.

### 2.2. Construction of LSMP Indices

We construct a daily LSMP index (LSMPi) for each meteorological variable mainly to make probabilistic predictions of precipitation. First, we choose a large spatial domain (100°E to 60°W and 20°S to 90°N) that captures the highly significant and consistent regions for the LSMPs. A large domain was used to ensure that we capture the full spatiotemporal extent of the LSMPs. Then we divide the years under consideration into training (NDJFM of 1948–1982) and verification years (NDJFM of 1982–2015). Corresponding to the training and verification periods, we divide all meteorological fields ($Y$) into training $\left(Y^T\right)$ and verification $\left(Y^V\right)$ sets. Then, we construct "training" LSMPs for a variable $Y^T$, $\overline{LY}_{l*}^{c,T}$ for each cluster $c$ as in Equation 1, where $*$ denotes lags 0–6. The LSMPi for a meteorological variable $\left(Y^T\right)$ in the training period $T$ is constructed by projecting $\overline{LY}_{l*}^{c,T}$ onto the corresponding daily $\left(Y^T\right)$ time series,

$$LSMPi_Y^{c,T} = \frac{\left(W\overline{LY}_{l*}^{c,T}\right)\left(WY^T\right)}{\left[W\overline{LY}_{l*}^{c,T}\right]^2}, \tag{2}$$

where $W$ is the weight assigned to each grid point based on both the normalized sign count (i.e., normalized by the number of events. Hence a sign count of 0.6 means 80% of the members have the same sign) and areal weighting accounting for the convergence of meridians. $LSMPi_Y^{c,T}$ is the daily product having dimensions of $lon \times lat$ for each cluster. The final daily LSMPi $\left(LSMPi_Y^{T}\right)$ is chosen by taking the maximum of the 4 $LSMPi_Y^{c,T}$, each computed for a cluster.

Similarly, the LSMPi for a meteorological variable $\left(Y^V\right)$ in the verification period $V$ is constructed by projecting $\overline{LY}_{l*}^{c,T}$ onto the corresponding daily $Y^V$ time series,

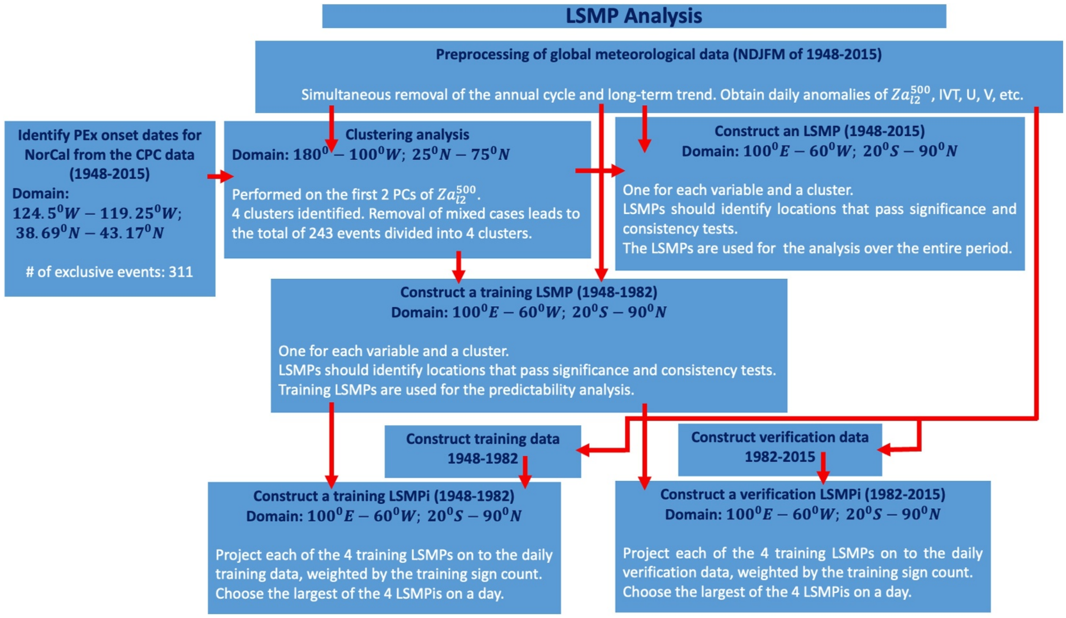

**Figure 1.** The infographic shows the steps involved in the large-scale statistically meaningful pattern (LSMP) analysis.

$$LSMPi_Y^{c,V} = \frac{\left(W\overline{LY}_{l*}^{c,T}\right)\left(WY^V\right)}{\left[W\overline{LY}_{l*}^{c,T}\right]^2}, \tag{3}$$

The final daily LSMPi $\left(LSMPi_Y^V\right)$ is constructed by taking the maximum of the four $LSMPi_Y^{c,V}$, each computed for a cluster. We use the same training LSMP $\overline{LY}_{l*}^{c,T}$ to compute LSMPi for training and verification data sets. The daily LSMPi measures how similar a given day is to a specific cluster mean LSMP.

The LSMP process explained above is summarized in the infographic shown in Figure 1.

### 2.3. Probabilistic Prediction of Precipitation Events Using LSMP Indices

To find useful predictors, we use quantile regression to predict the $95^{th}$ percentile of $\overline{P}$ using LSMPi as predictors. The LSMPi for each variable is constructed as described in Section 2.2. The fitness of each LSMPi predictor is estimated using a model selection criterion called the Akaike information criterion (AIC; Akaike, 1974). We also use a combination of two or more predictor variables to estimate if it produces a lower AIC than the individual AIC values. A suite of measures for assessing the prediction skill of LSMPi is used and associated with different meteorological variables. These measures of prediction skill are described in Table 1.

Of the atmospheric variables tested, we find that IVT at lag 2 is the best predictor of a PEx event, and adding any other variable to IVT does not significantly reduce the AIC. Therefore, we use LSMPi for IVT from the training and verification sets to make probabilistic predictions of precipitation. We use a copula framework to make a probabilistic prediction of PEx events. Copulas are mathematical functions that define the joint distributions of two or more random variables independent of their marginal distributions (AghaKouchak et al., 2010; Hao & AghaKouchak, 2013; Shojaeezadeh et al., 2018). We use a copula to define the conditional probability density of precipitation using the marginal distributions of an LSMPi and the joint distribution of the LSMPi and daily precipitation, as summarized below:

If $F(p) = y$ and $F(l) = x$ are marginal conditional distribution functions (CDFs) of daily precipitation ($P$) and an LSMPi ($l$), then there exists a copula function (C) that defines their joint CDF,

$$F(p,l) = C(F(p),F(l)) = C(y,x). \tag{4}$$

**Table 1**
*Contingency Table and Measures of Prediction Skills*

(a) Contingency table

| Forecast | Observed: Yes | Observed: No | Marginal total |
|---|---|---|---|
| Yes | (a) Hit | (b) False alarm | a + b |
| No | (c) Miss | (d) Correct negative | c + d |
| Marginal total | a + c | b + d | a + b + c + d |

(b) Prediction measures

$a^{*} = \frac{(a+b)(a+c)}{(a+b+c+d)}$

| Measures | Formula | Range [poor—good] |
|---|---|---|
| Probability of Detection (POD) | $\frac{a}{(a+c)}$ | [0,1] |
| False Alarm Ratio (FAR) | $\frac{b}{(a+b)}$ | [1,0] |
| Threat Score (TS) | $\frac{a}{(a+b+c)}$ | [0,1] |
| Gilbert Skill Score (GSS) | $\frac{(a-a^{*})}{(a-a^{*}+b+c)}$ | $[-\frac{1}{3},1]$; no skill = 0 |
| Pierce Skill Score (PSS) | $\frac{(ad-bc)}{(a+c)(b+d)}$ | [-1,1]; no skill = 0 |

*Note.* The observed and forecasted events are PEx >95$^{th}$ percentile.

The copula probability density function c(*) can be defined as:

$$c(y,x) = \frac{\partial^2 C(y,x)}{\partial y \partial x}. \tag{5}$$

From Equations 4 and 5, the conditional probability of precipitation ($P$) conditioned on the LSMPi ($l$) is defined as

$$f(p|l) = c(y,x)f(l), \tag{6}$$

where $f(l)$ is the PDF of the LSMPi($l$).

## 3. Results

### 3.1. Identifying Minimum Number of Clusters Using *k*-Means Clustering

We apply a k-means clustering algorithm to the 2 leading PCs of $Za_{l2}^{500}$ and compute the variance ratio as described in the methods section. The resulting variance ratio $R$ for 1–7 clusters is shown as a black curve in Figure 2a. We also compute the variance ratio for the synthetic data as described in the methods section; the 99$^{th}$ percentile of which ($R_{sig}$) is shown as the red dashed curve. A cluster number is considered significant at the 99% level if $R > R_{sig}$ (i.e., where a black circle is above the red line in Figure 2a). The figure suggests that a set of 3 clusters or more is statistically significant at the 99% significance level. To find the minimum number of robust clusters, we also perform a series of sensitivity tests to varying event detection criteria (e.g., varying precipitation threshold) and multiple spatial domain sizes. We find that a minimum of 4 clusters is statistically significant and robust.

In addition to significance and sensitivity tests, we also visually examine the cluster mean $Za^{500}$ patterns for $k = 3$, 4, and 5: shown in Figure 2b. Each cluster pattern for $k = 3$ is easily distinguished from other clusters and identified using an oval drawn with specific color and line. When going from $k = 3$ to 4 clusters, we find patterns quite similar to the previous three clusters again. It is worth noting that those three clusters are defined better than those for $k = 3$: magnitudes of the extrema are greater as are the sign counts. In addition, the new cluster is distinct from the other three patterns and has larger subtropical sign counts than any of the $k = 3$ cluster means. Therefore, $k = 4$ is a clear improvement over what we find for $k = 3$. Is there further improvement in choosing $k = 5$? When we go from $k = 4$ to 5, we find analogs to the four patterns of $k = 4$. Three of those four have similar magnitudes and sign counts as when $k = 4$. Only one of those four (blue oval of long dashes) has arguably larger sign counts. However, the new fifth pattern is problematic. First, its elements are very similar to two of the patterns found when $k = 4$. Second, it has weak sign counts. In short, it has weak separation from other clusters. Therefore, although significance testing indicates significantly different clusters are found for $k = 3$, 4, and 5, we narrow the choice to $k = 4$ by grounding the statistical analysis with LSMP maps.

The *k*-means clustering was applied to 311 events and the result is in Figure 2b. The *k*-means clustering is a hard clustering method, in that each member is entirely assigned to a cluster. However, events may resemble more than one cluster. In such cases, the membership of that event is not unequivocally defined. In an iterative procedure, we identified those mixed cases and removed them from the final clustering. This procedure further reduces the events from 311 to 243. The final cluster mean patterns in $Za^{500}$ using 243 events are shown in Figure 3. The k-means clustering divides the 243 precipitation events into 4 clusters of roughly equal sizes. Clusters 1–4 have 71, 70, 61, and 41 members, respectively. The PEx dates, along with cluster assignments, are listed in Supporting Information S1. Moore et al. (2021) applied fuzzy clustering to identify clusters of meteorological variables associated with Northern California PEx events. Fuzzy clustering assigns probability values to each member of the cluster. This allows any individual member to belong to more than one cluster. Our procedure ensures that only those members that have similar probabilities of being in more than one cluster are removed from the final set of clusters.

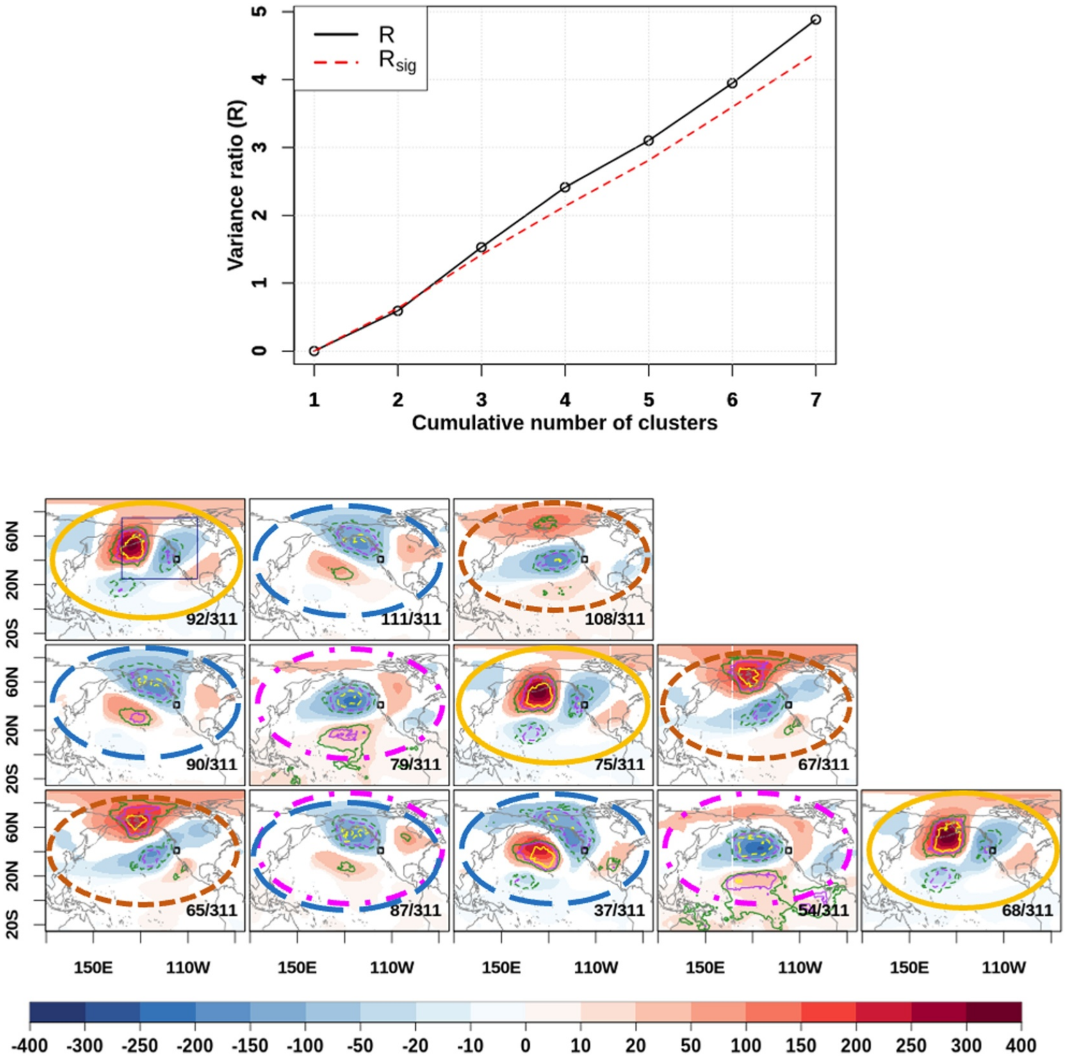

**Figure 2.** (a) Significance of $Za_{l2}^{500}$ clusters for cluster numbers 1–7. The $X$-axis shows the number of clusters for which the variance ratio ($R$) on the $Y$-axis is computed. The black curve shows variance ratio $R$ computed from $Za_{l2}^{500}$. The red curve shows the 99$^{th}$ percentile ($R_{sig}$) of the variance ratio computed from synthetic data generated using the Monte Carlo procedure. A cluster number is considered significant if $R > R_{sig}$. (b) Clustering of 500 hPa geopotential height anomalies, $Za_{l2}^{500}$ at lag 2. Top row: $k = 3$, Middle row: $k = 4$, Bottom row: $k = 5$. Shaded contours are plotted where significant at the 95% level (unit: m). The small square over Northern California on each panel is the NorCal region where the PEx occurs 2 days later. The ratio in the lower right corner of each panel shows the number of events in that cluster divided by the total number of events. Line contours show consistency via sign counts, where green equals 0.6 (meaning 80% of the ensemble members have the same sign at that point). Purple is 0.75 (87.5%) and yellow is 0.9 (95%). The colored ovals indicate the most similar pattern across different rows. However, three of the panels on the bottom row seem subjectively to mix two patterns on the middle row. In the top-left panel, the navy-colored rectangle shows the domain used for the clustering analysis.

The LSMP patterns shown here are similar to patterns shown in Moore et al. (2021). Using two EOFs of 500 hPa geopotential anomaly fields, they find four patterns, as well. However, their patterns are derived from time averages of the first 5 days of longer duration PEx events. Here, we show patterns 2 days *prior* to PEx event onset and include many more shorter-duration events. Noting these differences, our clusters 1–4 are most similar to their clusters C2, C1, C3, and C4, respectively. Our names for the patterns differ from those used by Moore et al. (2021) because: (a) We examine the patterns over a larger domain and (b) we emphasize the properties of the field used to define the clusters.

Our four clusters are described below with corresponding Moore et al. (2021) names in parentheses.

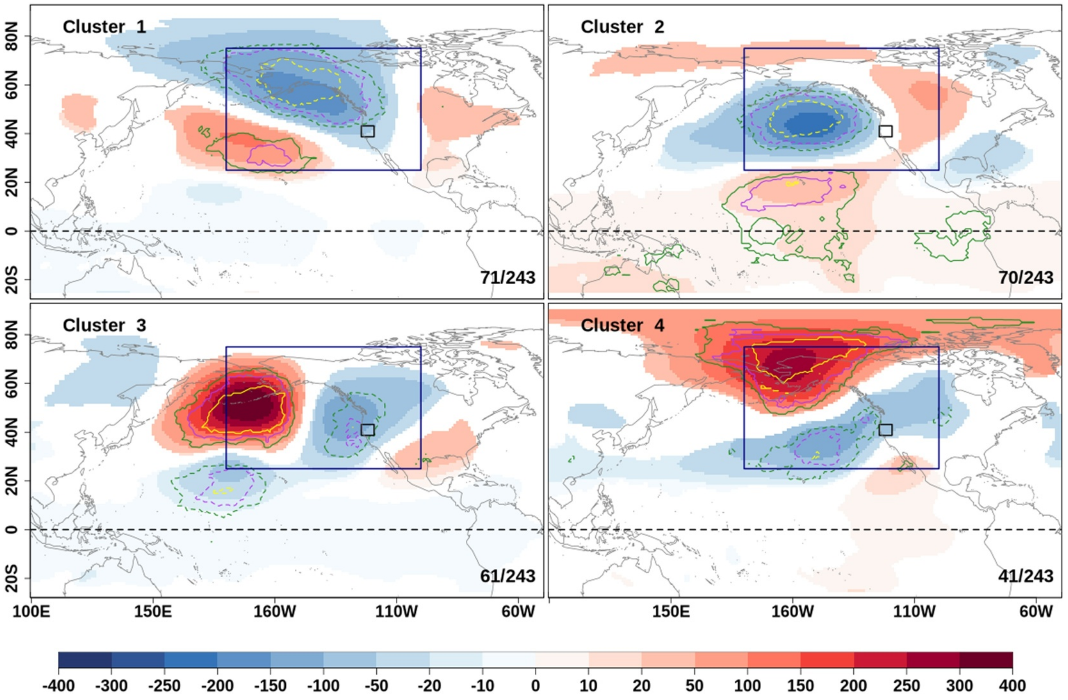

**Figure 3.** Large-scale statistically meaningful pattern clusters of $Za_{l2}^{500}$ (unit: m) 2 days prior to the PEx onset in a format similar to individual panels of Figure 2b. Events identified as "mixed" have now been removed from the analysis leaving 243 events tracked. The ratio in the lower right corner of each panel shows the number of events in that cluster divided by the total number of events tracked. Line contours show consistency via sign counts, where green means 80% of the ensemble members have the same sign at that point, purple is 87.5%, and yellow is 95%. The navy-colored large rectangle shows the domain used for the clustering analysis. The small black rectangle indicates the NorCal region. A dashed line marks the equator.

1. *Northwest continental negative height anomaly* (Poleward-shifted zonal jet) Cluster 1 has a large negative $Za_{l2}^{500}$ that extends over Alaska and the west coast of North America. Southwest of it, a positive anomaly occupies the midlatitude Pacific. Also present is a faint, low sign count, but significant positive anomaly over northeast North America.
2. *Eastward positive "PNA"* (equatorward-shifted zonal jet) Cluster 2 has a large negative geopotential anomaly centered over the northern Pacific co-occurring with a positive $Za_{l2}^{500}$ to the south over the central tropical Pacific. To the east, a significant, weak, low sign count wavetrain occurs: positive central Canadian and negative SE USA anomalies. Together the four anomalies look somewhat similar to the Pacific-North American (PNA; Barnston & Livezey, 1987; Leathers et al., 1991; Wallace & Gutzler, 1981) loading pattern, except that it has been phase shifted eastward. "PNA" in the cluster label is purely descriptive of the pattern and not intended to be equal to the actual PNA pattern.
3. *Westward negative "PNA"* (midlatitude blocking) cluster 3 has a low in the central subtropical Pacific and a Northwest-Southeast wavetrain with a very strong positive anomaly centered over the Aleutians, a strong negative anomaly near the Canadian west coast, and a weak, low sign count, positive anomaly over southeastern North America. These four anomaly centers may look like the PNA pattern (with negative sign), but this cluster pattern is shifted westward of the PNA loading pattern. Again, "PNA" in the label is purely descriptive. This pattern nearly matches the California cold air outbreak (CAO) pattern (Grotjahn & Zhang, 2017) 2 days before the CAO.
4. *Prominent Alaskan ridge* (high-latitude blocking) cluster 4 has a prominent positive anomaly over Alaska and the adjacent Arctic Ocean. To the south-southeast, lies a negative anomaly and further south-southeast a weak positive anomaly extending across much of the tropical Pacific to subtropical Baja California.

Three broad conclusions can be drawn to this point. First, several prior works listed in the introduction looked at a smaller region, and all find a low pressure centered off the California coast. We also find an anomalous low pressure just off the coast in all of our PEx events. But, this low pressure differs greatly in shape between the clusters. Second, this low pressure is part of a much larger-scale pattern that can be grouped into four clusters. The spatial patterns associated with the PEx clusters extend over much of North America and the northern Pacific, even across the equatorial Pacific. Significant patterns over the tropical Pacific suggesting a tropical connection to rainfall extremes over Northern California. Third, each cluster mean in Figure 3 has patterns that are statistically significant (shading) and highly consistent (contours), the two essential features of an LSMP.

### 3.2. Evolution of Clusters

As expected from the title, this paper focuses on the concurrent evolution of cluster mean LSMPs during the 2 weeks before PEx onset. Some clusters can be traced backward in time much longer than other clusters. The figure descriptions are included to identify important features from which generalizations will be drawn. There are multiple potential uses for these LSMP details, such as: dynamical analysis, model assessment, model projections, and predictability. Probabilistic prediction is explored in Section 3.3.

To sample LSMP properties the following figures are discussed. Figure 4 shows 500 hPa streamfunction anomalies $\left(\Psi a^{500}\right)$; this field captures the patterns of atmospheric highs and lows and consequent flow, but is preferable to geopotential height for depicting flow patterns in the tropical and equatorial regions. The upper-level jet evolution is shown, with a focus on the zonal component at 300 hPa ($Ua^{300}$, Figure 5) supplemented by information from the meridional wind anomaly component $\left(Va^{300}\right)$ in Figure S14 in Supporting Information S2. We show the evolution of vertically integrated water vapor transport anomalies (IVTa) in Figure 6. Local minima in mean sea-level pressure anomaly (*SLPa*, Figure 7) are used to indicate the position of cyclones (Wernli & Schwierz, 2006), which guide low-level water vapor fluxes toward NorCal. Temperature anomalies at four levels are discussed in Supporting Information S2.

#### 3.2.1. Evolution of 500 hPa Streamfunction Anomalies $\left(\Psi \mathbf{a}^{500}\right)$

The evolution of 500 hPa streamfunction anomalies $\left(\Psi a^{500}\right)$ for the four clusters is shown in Figure 4. $\Psi a^{200}$ and $\Psi a^{850}$ are similar to that for $\Psi a^{500}$, and hence are not shown.

The cluster 1 pattern starts with a central North Pacific ridge anomaly roughly 5–6 days before the event onset. This ridge anomaly extends throughout the atmospheric column (being visible at 300 and 850 hPa levels). Northeast of it, a trough builds over Alaska and beyond: from NorCal northwestward to the Bering Strait. This low anomaly is very large and mainly over the continent, hence our label of NW continental negative height anomaly. That large trough anomaly is strongest the last 2 days before onset. At onset, a weak ridge anomaly forms over southwestern North America. This combination of anomalies, trough northwest and ridge southeast of the PEx region, supports a strong onshore flow over the PEx region.

Cluster 2 has a pair of anomalies: a mid-latitude trough centered near 50°N and a subtropical ridge near 20°N that emerge in the North Pacific almost two weeks before PEx onset. Both anomalies grow in size and strength over a 2-week time, with the slight eastward movement of the ridge-trough pattern. The orientation and location of the ridge-trough pattern in cluster 2 both differ from cluster 1, such that the trough anomaly in cluster 2 is located further south, over the North Pacific Ocean and partly over southwestern Canada. This trough anomaly is strongest 2 days before onset. In addition, the trough-ridge pattern in cluster 2 is oriented more N-S than in cluster 1.

In cluster 3, a stationary Aleutian ridge anomaly is observed in the 500, as well as in the 300 and 850 (not shown), hPa $\Psi a$ fields more than a week before onset, steadily strengthening until peak anomaly amplitude two days before onset. Two $\Psi a^{500}$ troughs develop, one to the south and the other to the east of the Aleutian ridge anomaly around a week before the onset. A secondary ridge in $\Psi a^{500}$ forms over northern Mexico and Southern CONUS a few days before the onset. This secondary anomalous ridge is much stronger and wider than in the two prior clusters. The four strong anomaly centers are superficially similar to the PNA pattern, but the whole pattern is shifted west by >20 degrees of longitude, thus prompting our label of Westward negative “PNA.”

For cluster 4, a positive anomaly in $\Psi a^{500}$ starts developing over northern Alaska about 8 days before PEx onset. This ridge prompts our cluster label: Prominent Alaskan ridge. This ridge anomaly expands westward until the onset, but it reaches peak amplitude over northern Alaska 2 days before onset. A low forms over the central North Pacific a few days later, which expands eastward across the North American west coast, forming a band of low

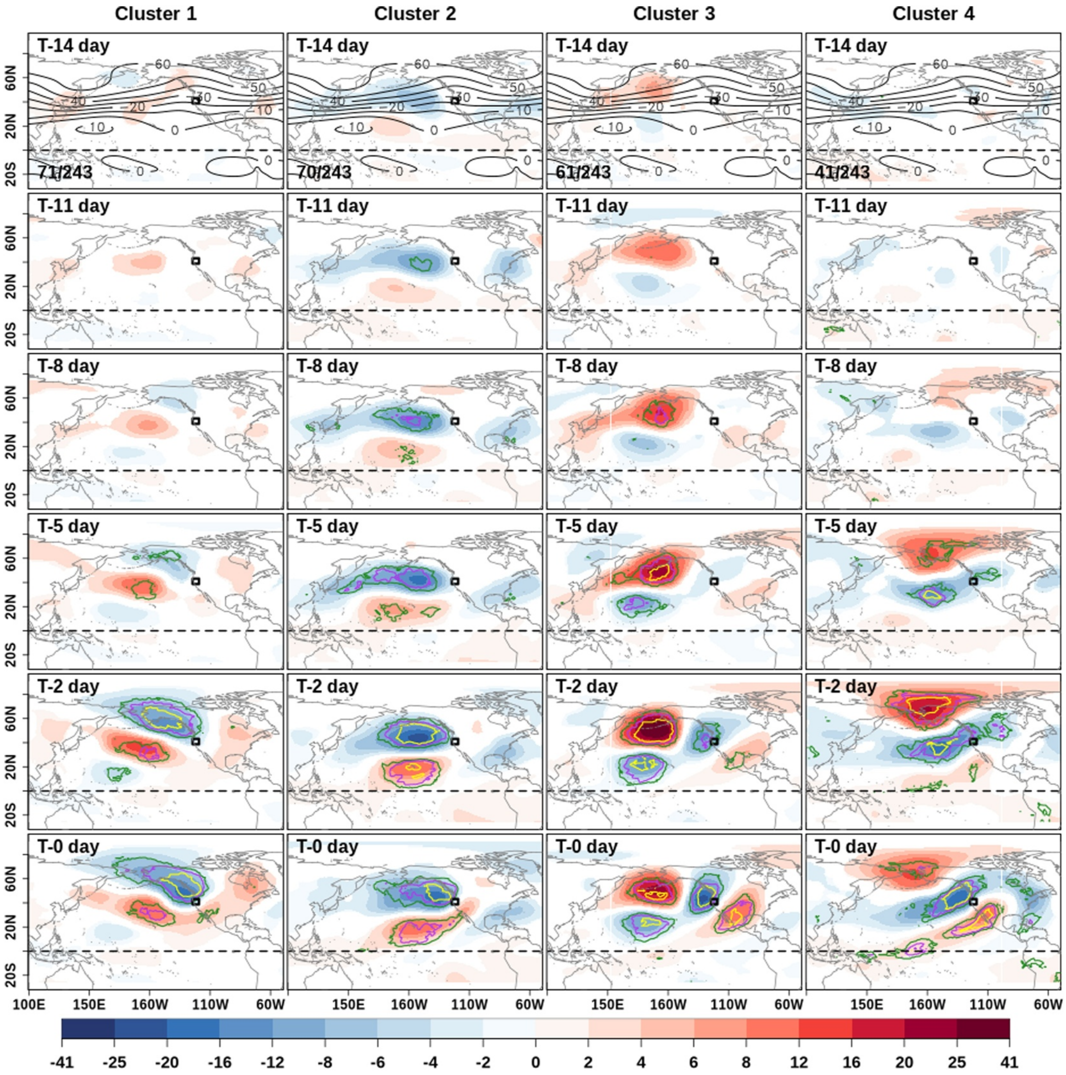

**Figure 4.** Evolution of 500 hPa streamfunction anomalies (unit:$10^6 m^2/s$). Shaded areas show anomalies significant at the 5% level. Contours show the consistency of the anomaly pattern. Green, magenta, and yellow contours show that at least 80%, 87.5%, and 95% of the cluster members have the same sign of anomalies, respectively. Solid black contours (contour interval: $10 \times 10^6 m^2/s$) in the top row show the climatological total streamfunction. The ratio in the lower-left corner of each top row panel shows the number of events in that cluster divided by the total number of events. The black rectangle indicates the NorCal region. A dashed line marks the equator.

pressure anomaly extending from the tropical Pacific Ocean across to north-central Canada. A secondary ridge anomaly is again centered over northern Mexico 2 days prior to the onset and extends southwestward into the tropical Pacific. Together, the anomalies form a ridge-trough-ridge pattern along the North American west coast.

In all four clusters, the most prominent and distinguishing features of each LSMP reach peak amplitude, significance, and consistency 2 days before onset. Furthermore, the cluster means differ less at onset than 2 days before; therefore, the best time for defining an LSMPi that separates the clusters is 2 days before onset.

### 3.2.2. Evolution of Upper-Level Jet $\left(Ua^{300}\right)$

The evolution of 300 hPa zonal wind anomaly field $\left(Ua^{300}\right)$ is shown in Figure 5. The meridional component wind anomaly at 300 hPa $\left(Va^{300}\right)$ is shown in Figure S14 in Supporting Information S2. Though not shown, the same fields at 200 hPa are virtually identical, giving us confidence in using Figure 5 to discuss jet stream properties.

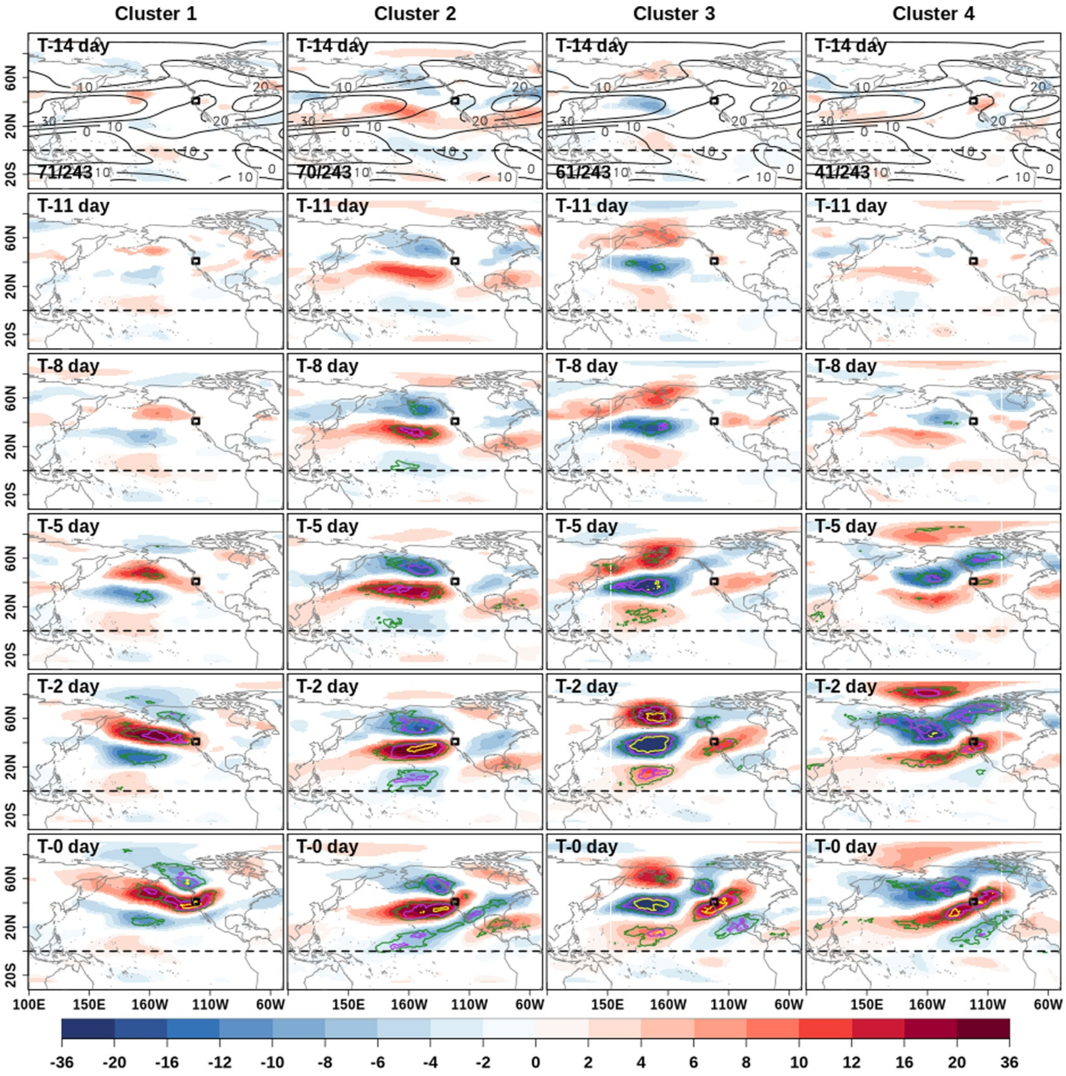

**Figure 5.** Same as Figure 4 but for the evolution of 300 hPa zonal wind anomalies (unit: m/s). Solid black contours (contour interval: 10 m/s) in the top rows show the climatological total zonal wind.

For cluster 1, beginning about 5–7 days prior to onset, there is a prominent dipole across much of the North Pacific. This dipole is centered mainly on the downstream end of the Asian subtropical jet. The effect of the dipole is to build the north side and reduce the south side of the jet mid-Pacific. As onset approaches, another negative anomaly (over northwest North America) appears. That negative anomaly along with the increasing amplitude and eastward extension of the positive anomaly results in a narrowing and dramatic strengthening of the jet over our NorCal focus region. Onshore zonal winds exceed 25 m/s at the focus region with an orientation that is from the southwest. The $Va^{300}$ pattern (Figure S14 in Supporting Information S2) shows comparable southerlies at and north of the NorCal region, giving the jet a SW-NE orientation there. The LSMPs are approximately equivalent-barotropic. Hence, the anomaly pattern for a wind anomaly component is similar at all levels from 850 through 300 hPa.

In cluster 2, the 300 hPa streamfunction anomalies (similar to the 500 hPa $\Psi_a$ in Figure 4) show that the NorCal region is sandwiched between a deep low to the north and a narrow ridge to the south at the onset. Hence, zonally-elongated 300 hPa zonal wind anomalies are oriented southwest-northeast up to two days before onset. A tripolar pattern by day 2 is similar to that in cluster 1, except the meridional spread is larger. A result is the positive anomaly of cluster 2 is nearly at the same latitude as a negative anomaly in cluster 1. Moreover, unlike cluster 1, these anomalies are apparent 10–11 days prior to onset. These anomalies: move the mid-Pacific jet axis southward, then extend the jet eastward (at about 35°N), narrow the latitude spread, and strengthen the jet stream over the eastern North Pacific. At onset, the positive zonal wind anomaly is strongly onshore, and the jet has a southwest orientation at the NorCal region, locally similar to but stronger than cluster 1.

In cluster 3, a tripolar zonal wind anomaly appears more than a week before onset. This tripolar pattern looks superficially similar to that in cluster 2 except with the opposite sign. A key difference is: the centers are roughly 25° longitude further west. Starting about 6 days before onset, a dipole appears over western North America, including a positive westerly anomaly over NorCal. The main negative anomaly is centered on the climatological subtropical jet, causing it to broaden in latitude. As onset approaches, the two southern positive anomalies join, suggesting a flow from lower latitudes than the prior two clusters. The meridional wind component (Figure S14 in Supporting Information S2) has strong southerlies centered over Kamchatka and the NorCal region, with northerlies in between (Gulf of Alaska). So, the jet stream winds at NorCal are again southwesterly.

In cluster 4, longitudinally broad bands of zonal wind anomalies appear 5 days before onset. Westerlies are enhanced in the subtropics and over the Arctic Ocean. A large negative anomaly covers much of the middle latitudes, especially 2 days before onset. In the mid-Pacific, the climatological position of the subtropical jet is centered midway between the negative anomaly and the southern positive anomaly. The net effect of the anomalies is to build the subtropical jet on its equatorward side. Downwind the anomaly curls northward creating strong southwesterly flow at the NorCal region. The meridional component is again strongly positive at the North American west coast.

Although the pattern of strong westerly flow (from a southwesterly orientation) at the NorCal region is *locally* very similar in all four clusters, how that local pattern is created differs greatly elsewhere, especially over the North Pacific.

### 3.2.3. Evolution of Integrated Vapor Transport Anomalies (IVTa)

Climatological total IVT (Figure S15 in Supporting Information S2) has two major positive bands: eastward flux oriented WSW to ENE across the North Pacific (from 30 to 40°N) and a tropical band of westward IVT centered at 15°N in the western Pacific. There is a relative minimum along the Baja coast. Each cluster mean has a strong onshore flow from the SW at NorCal. So, IVTa for each cluster must be large over the NorCal region to overcome the climatological low IVT.

Figure 6 shows IVTa and 850 hPa horizontal wind anomaly vectors. In cluster 1, a pair of zonal bands of positive IVTa form in the Pacific consistent with a positive streamfunction anomaly centered at 30°N. During the 2 days before PEx onset, the northern positive anomaly is driven toward the NorCal coast by the intensifying low pressure along the Canadian coast. This positive anomaly becomes confined close to the North American west coast and IVTa peaks over the NorCal region with a SW to NE orientation at onset. Negative IVTa covers a very large region northwest of NorCal, including all of Alaska. This large negative area is consistent with cold air advection as presumed from the northeasterly flow (850 hPa wind vectors). In turn, the cold advection supports the large negative 500 hPa streamfunction in Figure 4.

In cluster 2, a roughly zonal band of strongly positive IVTa develops along 35°N more than a week before the onset date, consistent with the cyclonic circulation visible in Figure 4. This band looks similar to cluster 1 but its peak values are further east and moving more slowly during the 2 days before onset. The IVTa further intensifies and bends northeastward along the continental coast. Total IVT is shown in Figure S15 in Supporting Information S2. Similar to cluster 1, the moisture travels > 70° longitude across the North Pacific. As with cluster 1, the *local* IVTa is again strongest and oriented SW-NE over NorCal. There is negative IVTa northwest of the NorCal region but it is less extensive and south of the location in cluster 1. The associated northeasterly flow brings cold air off Alaska, supporting the negative streamfunction anomaly there.

Cluster 3 IVTa develops broad, significant, and consistent areas a week before onset. Somewhat opposite to cluster 2, a positive anomaly develops near the Aleutians. To the south and east a large negative anomaly forms, along 35–40°N arcing poleward into Canada. These two anomalies may be anticipated from flow around the equivalent-barotropic anomalies of $\mathbf{\Psi a}^{500}$ (and SLPa shown next). Unlike opposite-signed anomalies in cluster 2, these two anomalies stay in place, consistent with other variables, such as Figure 4. In addition, consistent with prior figures, an intense positive IVTa develops close to the California coast (as well as a notable positive area in the tropics) only within 2 days before onset. Hence, although clusters 2 and 3 look like the "PNA" pattern shifted

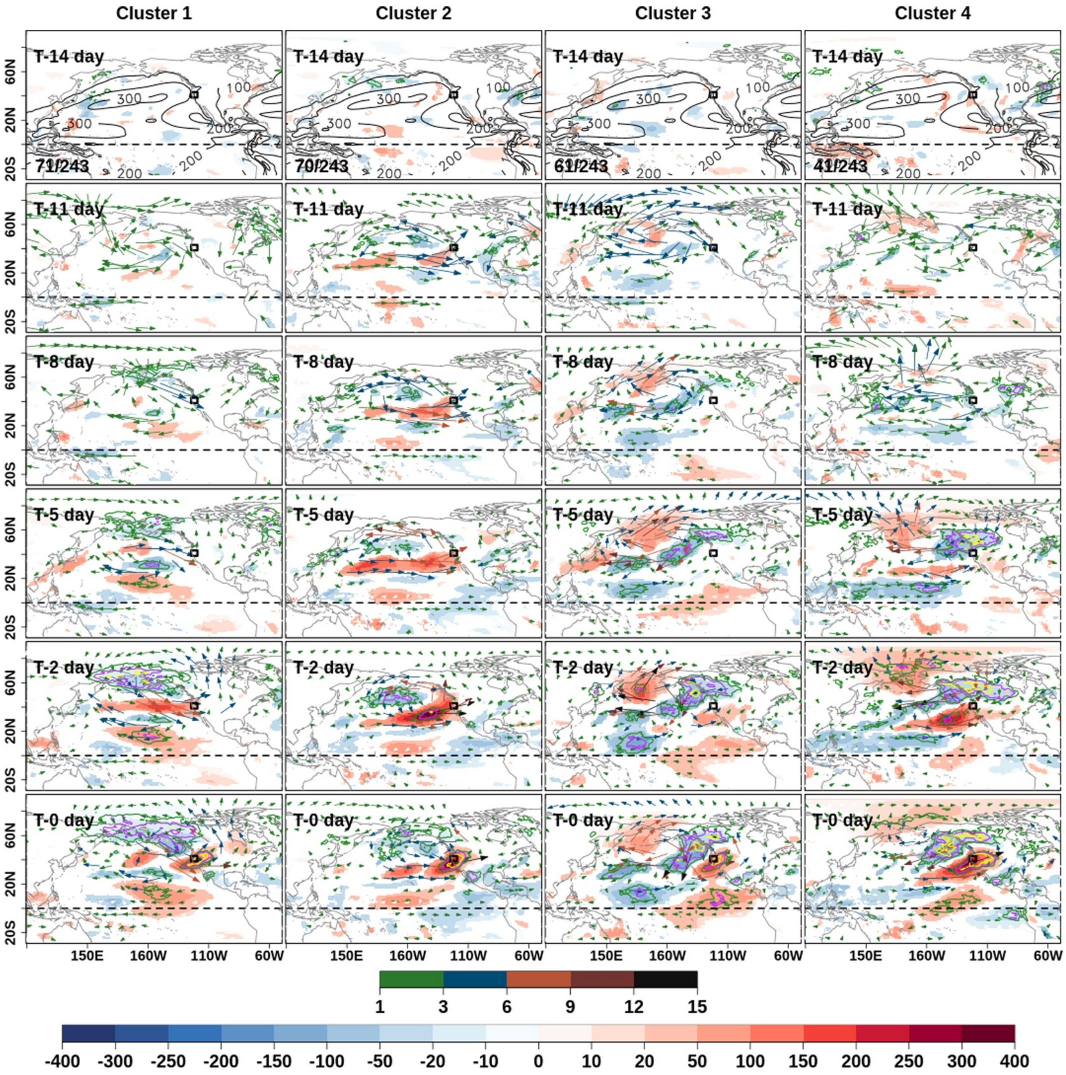

**Figure 6.** Same as Figure 4 but for the evolution of integrated vapor transport (IVT) anomalies (shading; unit: kg/m-s). Solid black contours (contour interval: 100 kg/m-s in the top rows show the climatological total IVT. The vectors show the 850 hPa wind anomalies (unit: m/s). The upper color bar at the bottom pertains to the 850 hPa wind anomalies and the lower color bar to the IVT anomalies.

east and west respectively, positive IVTa at NorCal is present >5 days before onset in cluster 2, but only a day before onset in cluster 3. Moreover, although all clusters have positive IVTa at and adjacent to the CONUS coast, IVTa is negative to the west and southwest of that area in this cluster. In contrast with cluster 2, where a large positive IVTa anomaly travels eastward from beyond the dateline, the moisture source now is much closer to and southwest of NorCal, reflecting how this LSMP develops in place.

The moisture transport anomaly pattern in cluster 4 has similarities intermediate to those in clusters 2 and 3. Visible from day T-5 to onset, cluster 4 has a positive anomaly like cluster 2 that moves eastward several days before onset except it is now 5° further south. Cluster 4 is similar to cluster 3 in having a persistent negative anomaly where climatological IVT is the largest along the Canadian coast. Also like cluster 3, a large positive anomaly off Baja California occurs and extends across the equator. However, the enhanced transport crossing the California coast has its origin just north of Hawaii about 5 days before onset.

Notably, the local pattern of IVTa at onset is very similar in all clusters over the NorCal region: sign count locally largest and have a SW to NE orientation. These results are consistent with Hecht and Cordeira (2017), who show that more extreme precipitation occurs along the California north coast and interior for south/southwesterly ARs than for westerly ARs. As with other variables, the LSMP properties elsewhere differ markedly, especially 2 days before onset. Where cluster 2 and cluster 1 (a bit further north for the latter) have positive anomaly mid-Pacific, cluster 3 (and to some extent cluster 4) has negative anomaly there. Clusters 3 and 4 appear to have an obvious connection to subtropical latitudes, whereas moisture transport in cluster 1 is more zonal at a much higher latitude. These differences between the patterns are less visible at the onset.

#### 3.2.4. Evolution of Sea Level Pressure Anomalies (*SLPa*)

Figure 7 shows *SLPa* evolution. The LSMPs are similar to Figure 4 due to the approximately equivalent-barotropic nature of the LSMPs. However, there are notable differences. To reduce the repetition of earlier comments, this subsection emphasizes the differences. A noticeable difference is the offset of negative *SLPa* anomalies from corresponding $Za^{500}$ anomalies at onset near the NorCal region (most other anomalies have a negligible offset). Such an offset is consistent with observed extratropical cyclogenesis wherein vertical tilt develops as upper and lower troughs, previously without vertical tilt, interact (Grotjahn, 1996; Grotjahn & Tribbia, 1995). Each NorCal PEx is associated with such a storm.

In cluster 1, a positive *SLPa* develops in the subtropical mid-Pacific around a week before the onset. This anomaly slowly expands eastward. A few days before onset, a low pressure anomaly over Alaska and western Canada forms in essentially the same location as at 500 hPa. The low pressure anomaly moves southeastward to become 20°east of the 500 hPa location at onset. Southwesterly flow around that trough drives surface air onshore over NorCal.

The cluster 2 SLPa LSMP has a large low anomaly south of Alaska, much like the streamfunction anomaly in the mid and upper atmosphere. But unlike the upper air patterns (e.g., Figure 4) the prominent high anomaly in the subtropics is missing. The negative SLPa low forms on the southeastern quadrant of the climatological atmospheric trough in the North Pacific. This low develops 11 days before onset. It subsequently strengthens and moves eastward until the anomaly is centered over the Canadian and NW USA west coast at onset, about 5° east of the 500 hPa position. Although cluster 1 has a similar low at onset, the time of formation is >10 days earlier and movement of the anomaly is eastward (instead of southeastward) for cluster 2. As with cluster 1, the anomaly fosters onshore surface flow over the NorCal region.

The cluster 3 LSMP is dominated by high SLPa centered just south of the Aleutians >10 days before onset. This anomaly is stationary and strengthens until day T-2 then wanes; it occurs through the depth of the troposphere. By day T-5, a stationary, weak low appears west of Hawaii, near the dateline, much weaker than its upper air counterpart. Only 2 days before onset the trough NW of NorCal appears, ∼5°SE of the upper troposphere trough. As in clusters 1 and 2, this anomaly would drive onshore surface winds, but this trough has a much smaller footprint. High SLP from the Great Lakes to Hudson Bay appears at onset; it is ∼10° east and much weaker than its upper air analog.

Cluster 4 has two dominant features. (a) A strong, large SLPa high over Alaska and NW Canada develops from day T-8 to day T-2, then diminishes by onset. (b) A trough in the subtropical eastern Pacific strengthens as it moves northeastward from day T-5 to onset; it moves onshore ∼10° SE of the upper level trough at onset. This SLPa trough has a different orientation than other clusters in that it has a trailing portion extending SW into the subtropics. Therefore, as with other variables, the pattern near the NorCal region at onset is similar in all four clusters, but elsewhere the patterns are quite different and especially strong at day T-2.

### 3.3. Probabilistic Predictions of Precipitation Extremes Using LSMPi as Predictors

This subsection shows some tests using individual LSMPi values, both at and prior to onset, to predict heavy precipitation values. As described in Section 2.2, we construct LSMPs from two periods of data: training LSMPs $\overline{LY}_{l*}^{c,T}$ and verification LSMPs $\overline{LY}_{l*}^{c,V}$ and do so for 0–6 days prior to onset. The training period is 1948–1982, whereas the verification period is 1982–2015; both periods use NDJFM months. We find that the LSMP clusters in the training and verification data are similar in spatial pattern, significance and consistency, an example of which is shown in Figure S20 in Supporting Information S2. The strong resemblance between the training and verification LSMPs supports the robustness of the *patterns* irrespective of the different training and verification periods. Less important to the discussion here is that we find more variation in the *frequency* of each cluster type.

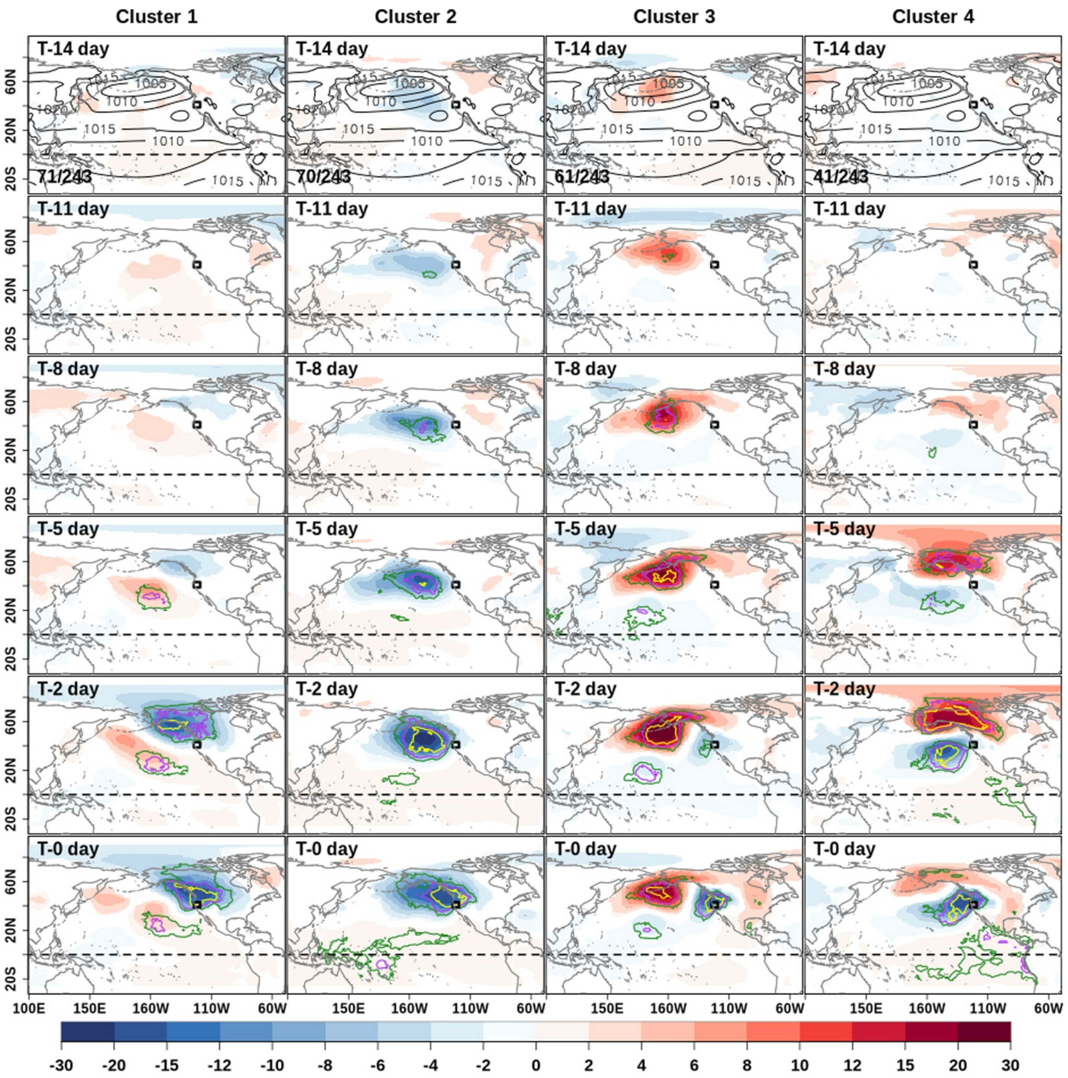

**Figure 7.** Same as Figure 4 but for the evolution of sea-level pressure anomaly (unit: hPa). Solid black contours (contour interval: 10 hPa) in the top rows show the climatological total sea-level pressure.

The numbers in clusters 1 and 2 are similar in both periods, but there are fewer members in clusters 3 and 4 in the verification period. We do not explore climate change issues in this report.

As described in Section 2.3, we constructed training and verification LSMPis from daily anomalies of the atmospheric variables that show large-scale synoptic patterns prior to the PEx onset. The tested variables are anomalies of 500 hPa geopotential height $\left(Za^{500}\right)$, 500 and 850 hPa air temperatures ($Ta^{500}$ and $Ta^{850}$), 850 hPa zonal and meridional winds ($Ua^{850}$ and $Va^{850}$), sea-level pressure ($SLPa$), skin temperature ($Ts$), precipitable water ($PWa$) and $IVTa$. Our discussion of relative skill emphasizes metrics designed for binary predictions. Although statistically valid, such measures are not ideal for this problem because near misses are not distinguished from large misses. As noted in Grotjahn (2011) there is more forecast value in near misses than large misses.

Table S1 in Supporting Information S1 shows measures of prediction skills when using LSMPis as predictors of extreme precipitation at lag 0 (and lag 2, in parenthesis). It is apparent that for all these variables, hits exceed misses by a large margin, indicating that the LSMPis can capture occurrences of PEx events very well. Of course, the skill decreases as the lag increases. But the LSMPis do so well that even at 2 days lag, they forecast the event occurrence with high accuracy. For all the variables, the probability of detection (POD) at lag 0 is 0.74 or more

(0.52 at lag 2). The maximum POD is offered by IVT at lags 0 (0.89 for training and 0.78 for verification data). It is worth noting that the false alarm ratio (FAR) ($FAR = FA/(hits + FA)$) is comparable to the POD for each variable. However, assessing the forecast skill by comparing POD with FAR may be misleading because the predictands (extreme precipitation events) are rare by definition (occurring less than 5% of the time). As explained in Ebert and Milne (2022), the evaluation of forecast skill based upon proportion-correct measures is not appropriate for predicting rare events. The TS score and Gilbert skill score are much lower than the PSS values for each variable. Ebert and Milne (2022) highlight the discrepancy among different skill scores when making forecasts for rare events. They suggest that the Pierce skill score is the only skill score that meets all three adequacy constraints for a proper measure of skill in rare events. It is worth noting that the forecast skills for training and verification data are comparable, and there is no drastic fall in forecast skills when LSMPi is constructed by projecting the training LSMPs (constructed for the period NDJFM of 1948–1982) onto the daily meteorological fields over an independent (verification) period (NDJFM of 1982–2015). Integrated vapor transport is superior in each of the metrics, which is perhaps unsurprising given that all the LSMPs show an AR-like pattern over the PEx region. Similarly, other studies of the circulation close to the PEx region have strong IVT around the south side of a trough that is unusually far south (e.g., D. Chen et al., 2021; Grotjahn & Faure, 2008).

**Table 2**
*Cumulative Ordering of Variables (LSMPis) According to Their Fitness as Predictors of the PEx Events at Different Lags in the Training Data Set*

| Cumulative ordering based on AIC | lag 6 | lag 4 | lag 2 | lag 1 | lag 0 |
|---|---|---|---|---|---|
| 1 | *PW* | *PW* | *IVT* | *IVT* | *IVT* |
| 2 | *SLP* | $U^{850}$ | *PW* | *SLP* | $U^{850}$ |
| 3 | *IVT* | $V^{850}$ | $U^{850}$ | *PW* | *PW* |
| 4 | $U^{850}$ | *IVT* | $V^{850}$ | $U^{850}$ | *SLP* |
| 5 | $T^{850}$ | *SLP* | *SLP* | $V^{850}$ | $V^{850}$ |
| 6 | $V^{850}$ | $T^{850}$ | $T^{500}$ | $Z^{500}$ | $Z^{500}$ |
| 7 | $T^{500}$ | $Z^{500}$ | $Z^{500}$ | *Ts* | $T^{500}$ |
| 8 | $Z^{500}$ | $T^{500}$ | *Ts* | $T^{500}$ | $T^{850}$ |
| 9 | *Ts* | *Ts* | $T^{850}$ | $T^{850}$ | *Ts* |

*Note.* The predictors are added cumulatively. The ordering shows the best predictor (or predictor combination), based on AIC, each time a set of predictors is tested. Refer to the text for more details. The variables shown are anomalies but the subscript "a" has been removed for brevity here.

Table S1 in Supporting Information S2 includes the AIC, which is a measure of the fitness of a variable as a predictor of PEx events. When comparing two variables, a variable with a lower AIC is considered a better predictor. Table 2 indicates that the most skillful predictive combination of variables varies with lag. In the subsequent discussion, the subscript "a" has been dropped. For example, for lag 0, IVT is the best single predictor, then the best combination for two predictors is IVT with $U^{850}$. For three and four predictors, add PW then SLP in the training data set. However, for lag 2, prediction is best when IVT is followed by PW (and then $U^{850}$) when two (and then three) predictors are used, respectively, in the training data set. Hence, IVT + $U^{850}$ + PW is the best combination of three variables at lag 0. How many predictor variables together can best predict the PEx events based on our binary metrics**?** Figure 8 shows prediction skill metrics in the training and verification time periods for different numbers of predictor variables at lags 0–6. The same combinations of predictor variables (as in Table 2) are used for predicting PEx events in the training and verification time periods. The fitness criteria of predictors, AIC, shows that for shorter lead times (0–2 days), AIC is minimum for a combination of 3–4 predictor variables, suggesting that the combination of 3–4 of our predictor variables fits the prediction model best, and adding any more variable either adds no further improvement or possibly degrades the prediction. For longer lead time (4–6 days), AIC varies little with the number of predictors, though some other metrics do best with at least 3 or 4 predictors. The forecast skill based upon PSS suggests that the forecast skill is best for a combination of 3–4 variables for lags 1–6. But there is little improvement in prediction skills when using more than one predictor for lag 0 in the verification data. A comparison of the left and right columns in Figure 8 suggests that the fitness of predictor variables degrades a bit when the combination of predictor variables based upon training data is used to predict PEx events in the verification set. Similarly, the prediction skills are slightly degraded for verification data. However, there is no drastic fall in prediction skill (PSS) when compared with the training data. Moisture-based variables such as IVT or PW are the best predictors at any lag. Moreover, lower-level atmospheric variables (e.g., $U^{850}$) are better predictors than mid-level atmospheric variables (e.g., $T^{500}$). Most notably, IVT is the best predictor until 2 days before the onset but is the third best predictor nearly a week before the onset (lag 6). This analysis suggests that LSMPs do offer predictability of PEx events, but one must select the suitable variable depending on how far in advance one wants to make a prediction.

Figure 9a shows the probabilistic prediction of precipitation using lag 0 IVT LSMPi as a predictor of PEx in the training data set. The IVT LSMPi and PEx have a significant (at the 5% level) correlation of 0.43 based on Spearman's rank correlation test. Out of the 23 copulas tested, we find that the Joe copula performs the best based on maximum likelihood estimates. Therefore, we use the Joe copula to make predictions of the precipitation values. In the figure, the vertical color bars show the likelihood of predicted values, so the yellows indicate low

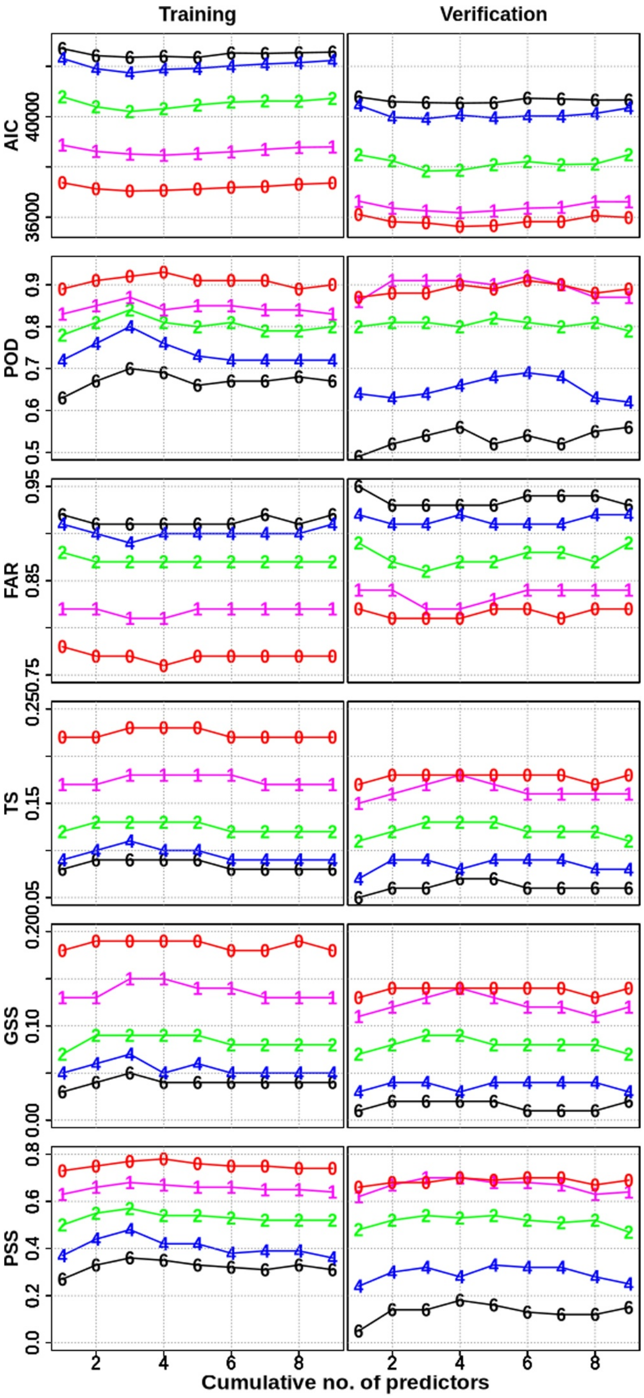

**Figure 8.** Prediction skill measures for combinations of LSMPi predictors. The *x*-axis shows the cumulative number of predictors, whereas the individual lines are for lags 0, 1, 2, 4, and 6. The LSMPi predictors (LSMPis) are combined using the order as shown in Table 2. Training period: NDJFM of 1948–1982; verification period: NDJFM of 1982–2015.

likelihood, and blues indicate a high likelihood of the predicted precipitation values. The figure shows that LSMPi constructed from IVT can predict the observed precipitation values (red dots) with high likelihood as most of the observed precipitation values are within the highly likely region (likelihood ≥ 0.75). The uncertainties in these predictions are shown by the black dots, which show the 95% confidence interval of the predicted values. Almost all of the observed extreme precipitation values lie within the 95% confidence interval. Figure 9b shows the predictions of PEx events based on the verification data. As might be expected from the previous figure, the predictions in the verification data are not quite as good as in the training data, but they remain comparable to those in the training data. This analysis shows that the LSMPis are skillful predictors of extreme precipitation values when evaluated on independent data.

## 4. Summary and Conclusions

Previous studies show that there is more than one set of large-scale circulation patterns that create extreme precipitation (PEx) events over Northern California (NorCal). In some of the published works, the large-scale circulation patterns connected to PEx events (or any other extreme meteorological events) are loosely described as large-scale meteorological patterns (LSMPs). However, as defined by Grotjahn (2011), an LSMP is more than a simple composite or aggregate, and it must indicate what is important in that composite or aggregate. What is important must pass both a significance test and a consistency test (like sign counts). To emphasize these statistical tests, we rename "LSMP" to be large-scale statistically meaningful patterns, here associated with PEx over NorCal. These have been our broad objectives: First, we establish what the minimum number of LSMP clusters are for NorCal PEx events. Second, we identify what is consistent and significant in the LSMP clusters of meteorological variables leading to PEx events. Third, we present a framework for the probabilistic predictions of PEx events using LSMP-based indices (LSMPis) as predictors. Those aspects of the current study have never been examined before.

We identified 311 exclusive PEx events, defined as the 24-hr precipitation averaged over the NorCal region $\left(\overline{P}\right)$ greater than the $95^{th}$ percentile of $\overline{P}$ over the 1948–2015 period from the CPC data. We apply *k*-means clustering analysis to the first two principal components of 500 hPa geopotential height anomalies $\left(Za^{500}_{l2}\right)$ two days before the 311 PEx onset dates. The patterns are most strongly distinguishable 2 days before onset and that is why we chose that timeframe for the clustering. Our analysis, using both the statistical and heuristic methods, suggests that a minimum of four clusters can explain NorCal PEx events. To analyze clusters whose members are distinct from members in other clusters, we removed PEx events identified as "mixed cases." This procedure reduces the number of PEx events to 243. The four clusters are identified as (a) *northwestern continental negative height anomaly* that has a large negative geopotential height anomaly extending over Alaska, western Canada, and the NW CONUS, (b) *eastward positive "PNA"* that has a large negative $Za^{500}$ centered over the northern Pacific co-existing with a positive $Za^{500}$ to the south of it over the central tropical Pacific (between 20°N and 20°S) and a wavetrain to the east, (c) *westward negative "PNA"* pattern having a very strong positive $Za^{500}$ centered over the Aleutian region with low heights to the south over the subtropical Pacific and a wavetrain to the east that creates a strong $Za^{500}$ near the Canadian west coast. (d) *Prominent Alaskan ridge* that

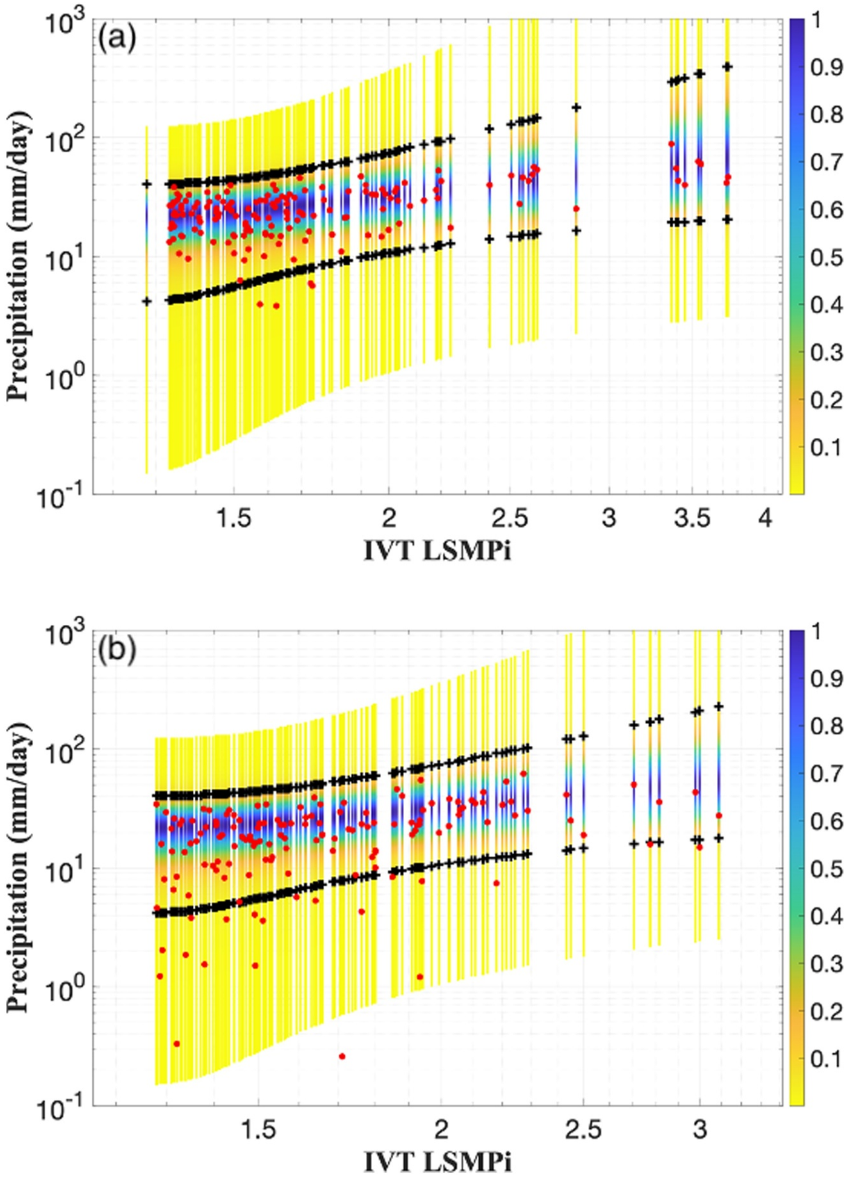

**Figure 9.** Probabilistic prediction of the precipitation amount (mm/day) using a single IVT LSMP index (IVT LSMPi) as a test. This test uses lag 0 data. Red dots show the observed precipitation values. Each vertical line represents the conditional marginal distribution of precipitation, color-coded based on the density values. The black dots mark the 95% range of predicted precipitation for that LSMPi value. (a): Training and (b): Verification data. The *Y*-axis uses a log-scale. The methods section provides details.

has a prominent positive $Za^{500}$ over Alaska and the adjacent Arctic Ocean with a trough across the midlatitude Pacific arcing into the NW CONUS.

The investigation of synoptic properties leading to PEx onset suggests that the LSMPs evolve differently from each other. The LSMP patterns near NorCal are essentially the same at PEx onset, but they have distinctly different patterns further away from the NorCal region and leading up to onset. For example, as the names of the clusters suggest, the streamfunction (and geopotential) anomalies have distinct spatial signatures in all four clusters. In addition, in two clusters a prominent part of the LSMP is present at least a week before onset, whereas other clusters develop their LSMPs only a couple of days before onset. Some clusters have nearly stationary anomalies that form the low pressure NW of NorCal, whereas other clusters have multiple features that travel large horizontal distances. The source of the moisture varies: from west of the dateline in the midlatitude Pacific, to ocean >30° west of NorCal, to the tropical Pacific near Hawaii, and in between. Though IVT anomalies (IVTa) at the onset have the same southwestern to northeastern orientation near NorCal for all clusters, cluster 2 and cluster 1 have positive IVTa mid-Pacific, whereas clusters 3 and 4 have negative IVTa there. Cluster 4 has a distinct stationary, warm lower tropospheric temperature anomaly over Alaska and much of the Arctic Ocean, in contrast, cluster 1 has a cold anomaly over the northeastern Pacific and Alaska that develops by onset. We find evidence that the NorCal PEx events have tropical connections, such as significant and consistent $Za^{500}$ south of 20°N crossing the Equator. Significant but not sufficiently consistent skin temperature anomalies hint at possible El Niño and La Niña influences on PEx events in clusters 2 and 3, respectively.

We estimated the predictive skills of LSMPis constructed from the training and verification periods. We constructed the LSMPi for a variable in the training and verification data by projecting the *training* LSMP onto the related daily variable in the training and verification data, respectively. Simple binary forecast metrics (e.g., POD, FAR, and PSS) show that the LSMPis have skills. Both capturing onset PEx as well as predicting PEx several days in advance. The best predictor tested was moisture-based with IVT being superior a day or two before onset. Moreover, lower-level variables we tested have superior prediction skill compared to middle or upper levels, at least up to 6 days before the onset. We tested the concept of using LSMPis to make probabilistic predictions of the amount of precipitation and found even one predictor has skill.

This work complements the existing literature on the NorCal PEx events, especially the work by Moore et al. (2021). Previous studies (e.g., Fish et al., 2022; Guirguis et al., 2019; Moore et al., 2021) show multiple "significant" synoptic patterns connected to the PEx events, for which we find comparable patterns. In this report, LSMPs are shown for the first time, specifically identifying where the members that comprised the LSMPs are highly consistent. Consistency is indicated by how often an anomaly of the same sign occurs at a grid point or location. Oftentimes, the more highly consistent locations are also where the anomaly magnitude in the LSMP is also larger (and significant). However, there are exceptions where the anomaly is highly consistent but not strong (e.g., subtropical central Pacific 500 hPa streamfunction in Cluster 1 at onset) or vice-versa (e.g., central Pacific IVT in Clusters 1, 2, and 3 at onset). We also introduce a rigorous statistical test to establish the minimum number of clusters needed for the clusters to be significantly different. The identification of the minimum number of clusters can help to facilitate future storyline-based simulations of extreme events resulting from multiple large-scale patterns. Moreover, this LSMP-based work provides a useful framework for the process-based evaluation of climate model simulations that can benefit both climate scientists (e.g., climate model development) and practitioners (e.g., climate model credibility for use in water resource management decisions). Additionally, since LSMPs are synoptic-scale patterns, they can be detected in coarse-resolution climate models. The LSMP patterns identified in this work can be used to evaluate climate models for applications such as model selection and multi-model weighting for future projections. Similarly, the indices that we test, one for each LSMP, can be further refined to better capture how well the two-dimensional spatial pattern on a specific day matches the shape and intensity of the corresponding LSMP. Since each index thereby collapses a two-dimensional pattern into a single number, one-dimensional time series tools can be applied to assess climate models. These LSMP-based assessments can be used to rank and weight models (on the specific skill in simulating NorCal PEx) and improve future projections of such extreme events.

Our work prompts further research. For example, as discussed in Reed et al. (2022) and shown by Palipane and Grotjahn (2018), LSMPs provide a useful metric for evaluating model skill. Our work suggests tropical teleconnections to the NorCal PEx events that could be further explored. We demonstrated that probabilistic prediction is feasible with LSMPis and the use of multiple LSMPis should be explored to improve such prediction, based on qualitative results in Grotjahn (2011). Potential future work could use the LSMP-based framework for model skill evaluations over the NorCal region, investigating changes in LSMPs in response to global warming, understanding the tropical impact on the NorCal PEx events, and designing storyline-based simulations to understand the effect of climate change on the historical large flood events over California (e.g., Michaelis et al., 2022; Rhoades et al., 2023). LSMPs in other time frames could be examined: Moore et al. (2021) find similar aggregates (not LSMPs) for 5-day averages that look similar to the LSMPs we show for 24-hr average PEx. LSMP analyses for PEx in other contexts could be explored such as rain versus snow-producing events. Finally, most of these questions could be explored for other regions of Earth.

## Conflict of Interest

The authors declare no conflicts of interest relevant to this study.

## Data Availability Statement

CPC Unified Gauge-Based Analysis of Daily Precipitation over CONUS data provided by the NOAA PSL, Boulder, Colorado, USA, from their website at https://psl.noaa.gov/data/gridded/data.unified.daily.conus.html (CPC, 1948-2024). Support for the Twentieth Century Reanalysis Project version 3 data set (20CRv3) is provided by the U.S. Department of Energy, Office of Science Biological and Environmental Research (BER), by the National Oceanic and Atmospheric Administration Climate Program Office, and by the NOAA Physical Sciences Laboratory. The 20CRv3 is available to download from https://www.psl.noaa.gov/data/gridded/data.20thC_ReanV3.html (20CRv3, 1836–2015).

**Acknowledgments**

This work is supported by the Department of Energy Office of Science award numbers DE-SC0016605, “A Framework for Improving Analysis and Modeling of Earth System and Intersectoral Dynamics at Regional Scales” and DE-AC02-05CH11231 for the CASCADE Scientific Focus (funded by the Regional and Global Model Analysis Program area within the Earth and Environmental Systems Modeling Program). Work conducted by PAU is under the auspices of the U.S. Department of Energy at Lawrence Livermore National Laboratory under contract DE-AC52-07NA27344. We sincerely thank Prof. Mojtaba Sadegh, Boise State University, Boise, ID, USA, for his valuable suggestions and MATLAB code for the copula analysis. We also thank Prof. David Straus, George Mason University, Fairfax, VA, USA for his guidance on the clustering analysis.

## References

20CRv3. (1836-2015). NOAA-CIRES-DOE 20th century reanalysis V3 [Dataset]. https://www.psl.noaa.gov/data/gridded/data.20thC_ReanV3.html

Agel, L., & Barlow, M. (2020). How well do CMIP6 Historical runs match observed Northeast U.S. precipitation and extreme precipitation–related circulation? *Journal of Climate*, *33*(22), 9835–9848. https://doi.org/10.1175/JCLI-D-19-1025.1

Agel, L., Barlow, M., Feldstein, S. B., & Gutowski, W. J. (2018). Identification of large-scale meteorological patterns associated with extreme precipitation in the US northeast. *Climate Dynamics*, *50*(5–6), 1819–1839. https://doi.org/10.1007/s00382-017-3724-8

AghaKouchak, A., Bárdossy, A., & Habib, E. (2010). Copula-based uncertainty modelling: Application to multisensor precipitation estimates. *Hydrological Processes*, *24*(15), 2111–2124. https://doi.org/10.1002/hyp.7632

Akaike, H. (1974). A new look at the statistical model identification. *IEEE Transactions on Automatic Control*, *19*(6), 716–723. https://doi.org/10.1109/TAC.1974.1100705

Akinsanola, A. A., Kooperman, G. J., Pendergrass, A. G., Hannah, W. M., & Reed, K. A. (2020). Seasonal representation of extreme precipitation indices over the United States in CMIP6 present-day simulations. *Environmental Research Letters*, *15*(9), 094003. https://doi.org/10.1088/1748-9326/ab92c1

Amini, S., & Straus, D. M. (2019). Control of storminess over the Pacific and North America by circulation regimes: The role of large-scale dynamics in weather extremes. *Climate Dynamics*, *52*(7–8), 4749–4770. https://doi.org/10.1007/s00382-018-4409-7

Barlow, M., Gutowski, W. J., Gyakum, J. R., Katz, R. W., Lim, Y.-K., Schumacher, R. S., et al. (2019). North American extreme precipitation events and related large-scale meteorological patterns: A review of statistical methods, dynamics, modeling, and trends. *Climate Dynamics*, *53*(11), 6835–6875. https://doi.org/10.1007/s00382-019-04958-z

Barnston, A. G., & Livezey, R. E. (1987). Classification, seasonality and persistence of low-frequency atmospheric circulation patterns. *Monthly Weather Review*, *115*(6), 1083–1126. https://doi.org/10.1175/1520-0493(1987)115⟨1083:CSAPOL⟩2.0.CO;2

Boroneant, C., Plaut, G., Giorgi, F., & Bi, X. (2006). Extreme precipitation over the Maritime Alps and associated weather regimes simulated by a regional climate model: Present-day and future climate scenarios. *Theoretical and Applied Climatology*, *86*(1–4), 81–99. https://doi.org/10.1007/s00704-005-0211-7

Chen, D., Norris, J., Goldenson, N., Thackeray, C., & Hall, A. (2021). A distinct atmospheric mode for California precipitation. *Journal of Geophysical Research: Atmospheres*, *126*(12), e2020JD034403. https://doi.org/10.1029/2020JD034403

Chen, M., Shi, W., Xie, P., Silva, V. B. S., Kousky, V. E., Wayne, H. R., & Janowiak, J. E. (2008). Assessing objective techniques for gauge-based analyses of global daily precipitation. *Journal of Geophysical Research*, *113*(D4). https://doi.org/10.1029/2007JD009132

Collow, A. B. M., Bosilovich, M. G., & Koster, R. D. (2016). Large-scale influences on summertime extreme precipitation in the northeastern United States. *Journal of Hydrometeorology*, *17*(12), 3045–3061. https://doi.org/10.1175/JHM-D-16-0091.1

Collow, A. B. M., Mersiovsky, H., & Bosilovich, M. G. (2020). Large-scale influences on atmospheric river–induced extreme precipitation events along the coast of Washington state. *Journal of Hydrometeorology*, *21*(9), 2139–2156. https://doi.org/10.1175/JHM-D-19-0272.1

Compo, G. P., Whitaker, J. S., & Sardeshmukh, P. D. (2006). Feasibility of a 100-year reanalysis using only surface pressure data. *Bulletin of the American Meteorological Society*, *87*(2), 175–190. https://doi.org/10.1175/BAMS-87-2-175

CPC. (1948-2024). CPC unified gauge-based analysis of daily precipitation over CONUS [Dataset]. https://psl.noaa.gov/data/gridded/data.unified.daily.conus.html

DeAngelis, A. M., Broccoli, A. J., & Decker, S. G. (2013). A comparison of CMIP3 simulations of precipitation over North America with observations: Daily statistics and circulation features accompanying extreme events. *Journal of Climate*, *26*(10), 3209–3230. https://doi.org/10.1175/JCLI-D-12-00374.1

Dettinger, M. D., Ralph, F. M., Das, T., Neiman, P. J., & Cayan, D. R. (2011). Atmospheric rivers, floods and the water resources of California. *Water*, *3*(2), 445–478. https://doi.org/10.3390/w3020445

Ebert, P. A., & Milne, P. (2022). Methodological and conceptual challenges in rare and severe event forecast verification. *Natural Hazards and Earth System Sciences*, *22*(2), 539–557. https://doi.org/10.5194/nhess-22-539-2022

Fish, M. A., Done, J. M., Swain, D. L., Wilson, A. M., Michaelis, A. C., Gibson, P. B., & Ralph, F. M. (2022). Large-scale environments of successive atmospheric river events leading to compound precipitation extremes in California. *Journal of Climate*, *35*(5), 1515–1536. https://doi.org/10.1175/JCLI-D-21-0168.1

Fujiwara, M., Wright, J. S., Manney, G. L., Gray, L. J., Anstey, J., Birner, T., et al. (2017). Introduction to the SPARC Reanalysis Intercomparison Project (S-RIP) and overview of the reanalysis systems. *Atmospheric Chemistry and Physics*, *17*(2), 1417–1452. https://doi.org/10.5194/acp-17-1417-2017

Gao, X., & Mathur, S. (2021). Predictability of U.S. regional extreme precipitation occurrence based on Large-Scale Meteorological Patterns (LSMPs). *Journal of Climate*, *34*(17), 7181–7198. https://doi.org/10.1175/JCLI-D-21-0137.1

Gao, X., Schlosser, C. A., Xie, P., Monier, E., & Entekhabi, D. (2014). An analogue approach to identify heavy precipitation events: Evaluation and application to CMIP5 climate models in the United States. *Journal of Climate*, *27*(15), 5941–5963. https://doi.org/10.1175/JCLI-D-13-00598.1

Gershunov, A., Shulgina, T., Ralph, F. M., Lavers, D. A., & Rutz, J. J. (2017). Assessing the climate-scale variability of atmospheric rivers affecting western North America. *Geophysical Research Letters*, *44*(15), 7900–7908. https://doi.org/10.1002/2017GL074175

Grotjahn, R. (1996). Composite trough evolution of selected west pacific extratropical cyclones. *Monthly Weather Review*, *124*(7), 1470–1479. https://doi.org/10.1175/1520-0493(1996)124%3C1470:CTEOSW%3E2.0.CO;2

Grotjahn, R. (2011). Identifying extreme hottest days from large scale upper air data: A pilot scheme to find California central valley summertime maximum surface temperatures. *Climate Dynamics*, *37*(3–4), 587–604. https://doi.org/10.1007/s00382-011-0999-z

Grotjahn, R., Black, R., Leung, R., Wehner, M. F., Barlow, M., Bosilovich, M., et al. (2016). North American extreme temperature events and related large scale meteorological patterns: A review of statistical methods, dynamics, modeling, and trends. *Climate Dynamics*, *46*(3–4), 1151–1184. https://doi.org/10.1007/s00382-015-2638-6

Grotjahn, R., & Faure, G. (2008). Composite predictor maps of extraordinary weather events in the Sacramento, California, region. *Weather and Forecasting*, *23*(3), 313–335. https://doi.org/10.1175/2007WAF2006055.1

Grotjahn, R., & Tribbia, J. (1995). On the mechanism of cyclogenesis as deduced from vertical axis tilts. *Tellus*, *47A*(5), 629–637. https://doi.org/10.1034/j.1600-0870.1995.00109.x

Grotjahn, R., & Zhang, R. (2017). Synoptic analysis of cold air outbreaks over the California Central Valley. *Journal of Climate*, *30*(23), 9417–9433. https://doi.org/10.1175/JCLI-D-17-0167.1

Guirguis, K., Gershunov, A., Clemesha, R. E. S., Shulgina, T., Subramanian, A. C., & Ralph, F. M. (2018). Circulation drivers of atmospheric rivers at the North American west coast. *Geophysical Research Letters*, *45*(22), 12–576. https://doi.org/10.1029/2018GL079249

Guirguis, K., Gershunov, A., DeFlorio, M. J., Shulgina, T., Delle Monache, L., Subramanian, A. C., et al. (2020). Four atmospheric circulation regimes over the North Pacific and their relationship to California precipitation on daily to seasonal timescales. *Geophysical Research Letters*, *47*(16), e2020GL087609. https://doi.org/10.1029/2020GL087609

Guirguis, K., Gershunov, A., Shulgina, T., Clemesha, R. E., & Ralph, F. M. (2019). Atmospheric rivers impacting Northern California and their modulation by a variable climate. *Climate Dynamics*, *52*(11), 6569–6583. https://doi.org/10.1007/s00382-018-4532-5

Gutowski, W. J., Decker, S. G., Donavon, R. A., Pan, Z., Arritt, R. W., & Takle, E. S. (2003). Temporal–spatial scales of observed and simulated precipitation in Central U.S. climate. *Journal of Climate*, *16*(22), 3841–3847. https://doi.org/10.1175/1520-0442(2003)016⟨3841:TSOOAS⟩2.0.CO;2

Hao, Z., & AghaKouchak, A. (2013). Multivariate standardized drought index: A parametric multi-index model. *Advances in Water Resources*, *57*, 12–18. https://doi.org/10.1016/j.advwatres.2013.03.009

Hecht, C. W., & Cordeira, J. M. (2017). Characterizing the influence of atmospheric river orientation and intensity on precipitation distributions over North Coastal California. *Geophysical Research Letters*, *44*(17), 9048–9058. https://doi.org/10.1002/2017GL074179

Lamjiri, M. A., Dettinger, M. D., Ralph, F. M., & Guan, B. (2017). Hourly storm characteristics along the U.S. west coast: Role of atmospheric rivers in extreme precipitation. *Geophysical Research Letters*, *44*(13), 7020–7028. https://doi.org/10.1002/2017GL074193

Leathers, D. J., Yarnal, B., & Palecki, M. A. (1991). The Pacific/North American teleconnection pattern and United States climate. Part I: Regional temperature and precipitation associations. *Journal of Climate*, *4*(5), 517–528. https://doi.org/10.1175/1520-0442(1991)004⟨0517:TPATPA⟩2.0.CO;2

Lee, Y.-Y., & Grotjahn, R. (2016). California Central Valley summer heat waves form two ways. *Journal of Climate*, *29*(3), 1201–1217. https://doi.org/10.1175/JCLI-D-15-0270.1

Loikith, P. C., Lintner, B. R., & Sweeney, A. (2017). Characterizing large-scale meteorological patterns and associated temperature and precipitation extremes over the northwestern United States using self-organizing maps. *Journal of Climate*, *30*(8), 2829–2847. https://doi.org/10.1175/JCLI-D-16-0670.1

Long, C. S., Fujiwara, M., Davis, S., Mitchell, D. M., & Wright, C. J. (2017). Climatology and interannual variability of dynamic variables in multiple reanalyses evaluated by the SPARC Reanalysis Intercomparison Project (S-RIP). *Atmospheric Chemistry and Physics*, *17*(23), 14593–14629. https://doi.org/10.5194/acp-17-14593-2017

Michaelis, A. C., Gershunov, A., Weyant, A., Fish, M. A., Shulgina, T., & Ralph, F. M. (2022). Atmospheric river precipitation enhanced by climate change: A case study of the storm that contributed to California's Oroville dam crisis. *Earth's Future*, *10*(3), e2021EF002537. https://doi.org/10.1029/2021EF002537

Moore, B. J., White, A. B., & Gottas, D. J. (2021). Characteristics of long-duration heavy precipitation events along the West Coast of the United States. *Monthly Weather Review*, *149*(7), 2255–2277. https://doi.org/10.1175/MWR-D-20-0336.1

Moore, B. J., White, A. B., Gottas, D. J., & Neiman, P. J. (2020). Extreme precipitation events in Northern California during winter 2016–17: Multiscale analysis and climatological perspective. *Monthly Weather Review*, *148*(3), 1049–1074. https://doi.org/10.1175/MWR-D-19-0242.1

Neiman, P. J., Ralph, F. M., White, A. B., Kingsmill, D. E., & Persson, P. O. G. (2002). The statistical relationship between upslope flow and rainfall in California's coastal mountains: Observations during CALJET. *Monthly Weather Review*, *130*(6), 1468–1492. https://doi.org/10.1175/1520-0493(2002)130⟨1468:TSRBUF⟩2.0.CO;2

Neiman, P. J., Ralph, F. M., Wick, G. A., Lundquist, J. D., & Dettinger, M. D. (2008). Meteorological characteristics and overland precipitation impacts of atmospheric rivers affecting the west coast of North America based on eight years of SSM/I satellite observations. *Journal of Hydrometeorology*, *9*(1), 22–47. https://doi.org/10.1175/2007JHM855.1

Newell, R. E., Newell, N. E., Zhu, Y., & Scott, C. (1992). Tropospheric rivers? – A pilot study. *Geophysical Research Letters*, *19*(24), 2401–2404. https://doi.org/10.1029/92GL02916

Palipane, E., & Grotjahn, R. (2018). Future projections of the large-scale meteorology associated with California heat waves in CMIP5 models. *Journal of Geophysical Research: Atmospheres*, *123*(16), 8500–8517. https://doi.org/10.1029/2018JD029000

Payne, A. E., & Magnusdottir, G. (2014). Dynamics of landfalling atmospheric rivers over the North Pacific in 30 years of MERRA reanalysis. *Journal of Climate*, *27*(18), 7133–7150. https://doi.org/10.1175/JCLI-D-14-00034.1

Polade, S. D., Gershunov, A., Cayan, D. R., Dettinger, M. D., & Pierce, D. W. (2017). Precipitation in a warming world: Assessing projected hydro-climate changes in California and other Mediterranean climate regions. *Scientific Reports*, *7*(1), 10783. https://doi.org/10.1038/s41598-017-11285-y

Ralph, F. M., Neiman, P. J., Wick, G. A., Gutman, S. I., Dettinger, M. D., Cayan, D. R., & White, A. B. (2006). Flooding on California's Russian River: Role of atmospheric rivers. *Geophysical Research Letters*, *33*(13). https://doi.org/10.1029/2006GL026689

Reed, K. A., Goldenson, N., Grotjahn, R., Gutowski, W. J., Jagannathan, K., Jones, A. D., et al. (2022). Metrics as tools for bridging climate science and applications. *WIREs Climate Change*, *13*(6), e799. https://doi.org/10.1002/wcc.799

Rhoades, A. M., Jones, A. D., Srivastava, A., Huang, H., O'Brien, T. A., Patricola, C. M., et al. (2020). The shifting scales of western U.S. landfalling atmospheric rivers under climate change. *Geophysical Research Letters*, *47*(17), e2020GL089096. https://doi.org/10.1029/2020GL089096

Rhoades, A. M., Zarzycki, C. M., Inda-Diaz, H. A., Ombadi, M., Pasquier, U., Srivastava, A., et al. (2023). Recreating the California New Year's flood event of 1997 in a regionally refined earth system model. *Journal of Advances in Modeling Earth Systems*, *15*(10), e2023MS003793. https://doi.org/10.1029/2023MS003793

Shojaeezadeh, S. A., Nikoo, M. R., McNamara, J. P., AghaKouchak, A., & Sadegh, M. (2018). Stochastic modeling of suspended sediment load in alluvial rivers. *Advances in Water Resources*, *119*, 188–196. https://doi.org/10.1016/j.advwatres.2018.06.006

Shukla, S., Safeeq, M., AghaKouchak, A., Guan, K., & Funk, C. (2015). Temperature impacts on the water year 2014 drought in California. *Geophysical Research Letters*, *42*(11), 4384–4393. https://doi.org/10.1002/2015GL063666

Slivinski, L. C., Compo, G. P., Sardeshmukh, P. D., Whitaker, J. S., McColl, C., Allan, R. J., et al. (2021). An evaluation of the performance of the twentieth century reanalysis version 3. *Journal of Climate*, *34*(4), 1417–1438. https://doi.org/10.1175/JCLI-D-20-0505.1

Slivinski, L. C., Compo, G. P., Whitaker, J. S., Sardeshmukh, P. D., Giese, B. S., McColl, C., et al. (2019). Towards a more reliable historical reanalysis: Improvements for version 3 of the Twentieth Century Reanalysis system. *Quarterly Journal of the Royal Meteorological Society*, *145*(724), 2876–2908. https://doi.org/10.1002/qj.3598

Smith, B. L., Yuter, S. E., Neiman, P. J., & Kingsmill, D. E. (2010). Water vapor fluxes and orographic precipitation over Northern California associated with a landfalling atmospheric river. *Monthly Weather Review*, *138*(1), 74–100. https://doi.org/10.1175/2009MWR2939.1

Srivastava, A., Grotjahn, R., & Ullrich, P. A. (2020). Evaluation of historical CMIP6 model simulations of extreme precipitation over contiguous US regions. *Weather and Climate Extremes*, *29*, 100268. https://doi.org/10.1016/j.wace.2020.100268

Straus, D. M. (2018). Clustering techniques in climate analysis. In *Oxford research encyclopedia of climate science*. https://doi.org/10.1093/acrefore/9780190228620.013.711

Straus, D. M., Molteni, F., & Corti, S. (2017). Atmospheric regimes: The link between weather and the large-scale circulation. In C. L. E. Franzke & T. J. O'Kane (Eds.), *Nonlinear and stochastic climate dynamics* (pp. 105–135). Cambridge University Press. https://doi.org/10.1017/9781316339251.005

Swain, D. L., Langenbrunner, B., Neelin, J. D., & Hall, A. (2018). Increasing precipitation volatility in twenty-first-century California. *Nature Climate Change*, *8*(5), 427–433. https://doi.org/10.1038/s41558-018-0140-y

Swain, D. L., Tsiang, M., Haugen, M., Singh, D., Charland, A., Rajaratnam, B., & Diffenbaugh, N. S. (2014). The extraordinary California drought of 2013/2014: Character, context, and the role of climate change. *Bulletin of the American Meteorological Society*, *95*(9), S3.

Timmermans, B., Wehner, M., Cooley, D., O'Brien, T., & Krishnan, H. (2019). An evaluation of the consistency of extremes in gridded precipitation data sets. *Climate Dynamics*, *52*(11), 6651–6670. https://doi.org/10.1007/s00382-018-4537-0

Wallace, J. M., & Gutzler, D. S. (1981). Teleconnections in the geopotential height field during the Northern Hemisphere winter. *Monthly Weather Review*, *109*(4), 784–812. https://doi.org/10.1175/1520-0493(1981)109⟨0784:TITGHF⟩2.0.CO;2

Wernli, H., & Schwierz, C. (2006). Surface cyclones in the ERA-40 dataset (1958–2001). Part I: Novel identification method and global climatology. *Journal of the Atmospheric Sciences*, *63*(10), 2486–2507. https://doi.org/10.1175/JAS3766.1

White, A. B., Moore, B. J., Gottas, D. J., & Neiman, P. J. (2019). Winter storm conditions leading to excessive runoff above California's Oroville dam during January and February 2017. *Bulletin of the American Meteorological Society*, *100*(1), 55–70. https://doi.org/10.1175/BAMS-D-18-0091.1

Xie, P., Chen, M., Yang, S., Yatagai, A., Hayasaka, T., Fukushima, Y., & Liu, C. (2007). A gauge-based analysis of daily precipitation over East Asia. *Journal of Hydrometeorology*, *8*(3), 607–626. https://doi.org/10.1175/JHM583.1

Zhao, Y., Xu, X., Li, J., Zhang, R., Kang, Y., Huang, W., et al. (2019). The large-scale circulation patterns responsible for extreme precipitation over the North China plain in midsummer. *Journal of Geophysical Research: Atmospheres*, *124*(23), 12794–12809. https://doi.org/10.1029/2019JD030583

Zhu, Y., & Newell, R. E. (1998). A proposed algorithm for moisture fluxes from atmospheric rivers. *Monthly Weather Review*, *126*(3), 725–735. https://doi.org/10.1175/1520-0493(1998)126⟨0725:APAFMF⟩2.0.CO;2